

Dartmouth College

Dartmouth Digital Commons

Open Dartmouth: Published works by
Dartmouth faculty

Faculty Work

5-27-2013

Narrow-Line Region Gas Kinematics of 24 264 Optically Selected AGN: The Radio Connection

J. R. Mullaney
Durham University

D. M. Alexander
Durham University

S. Fine
Durham University

A. D. Goulding
Harvard-Smithsonian Center for Astrophysics

C. M. Harrison
Durham University

See next page for additional authors

Follow this and additional works at: <https://digitalcommons.dartmouth.edu/facoa>



Part of the [External Galaxies Commons](#)

Dartmouth Digital Commons Citation

Mullaney, J. R.; Alexander, D. M.; Fine, S.; Goulding, A. D.; Harrison, C. M.; and Hickox, R. C., "Narrow-Line Region Gas Kinematics of 24 264 Optically Selected AGN: The Radio Connection" (2013). *Open Dartmouth: Published works by Dartmouth faculty*. 1839.
<https://digitalcommons.dartmouth.edu/facoa/1839>

This Article is brought to you for free and open access by the Faculty Work at Dartmouth Digital Commons. It has been accepted for inclusion in Open Dartmouth: Published works by Dartmouth faculty by an authorized administrator of Dartmouth Digital Commons. For more information, please contact dartmouthdigitalcommons@groups.dartmouth.edu.

Authors

J. R. Mullaney, D. M. Alexander, S. Fine, A. D. Goulding, C. M. Harrison, and R. C. Hickox

Narrow-line region gas kinematics of 24 264 optically selected AGN: the radio connection

J. R. Mullaney,^{1,2★} D. M. Alexander,¹ S. Fine,¹ A. D. Goulding,³ C. M. Harrison¹
and R. C. Hickox⁴

¹*Department of Physics, Durham University, South Road, Durham DH1 3LE, UK*

²*Laboratoire AIM, CEA/DSM-CNRS-Université Paris Diderot, Irfu/Service d'Astrophysique, CEA-Saclay, Orme des Merisiers, F-91191 Gif-sur-Yvette Cedex, France*

³*Harvard-Smithsonian Center for Astrophysics, 60 Garden Street, Cambridge, MA 02138, USA*

⁴*Department of Physics and Astronomy, Dartmouth College, 6127 Wilder Laboratory, Hanover, NH 03755, USA*

Accepted 2013 April 29. Received 2013 April 9; in original form 2012 December 21

ABSTRACT

Using a sample of 24 264 optically selected active galactic nuclei (AGNs) from the SDSS DR7 data base, we characterize how the profile of the [O III] $\lambda 5007$ emission line relates to bolometric luminosity (L_{AGN}), Eddington ratio, radio loudness, radio luminosity ($L_{1.4\text{ GHz}}$) and optical class (i.e. broad/narrow-line Seyfert 1, type 2) to determine what drives the kinematics of this kpc-scale line emitting gas. First, we use spectral stacking to characterize how the average [O III] $\lambda 5007$ profile changes as a function of these five variables. After accounting for the known correlation between L_{AGN} and $L_{1.4\text{ GHz}}$, we report that $L_{1.4\text{ GHz}}$ has the strongest influence on the [O III] $\lambda 5007$ profile, with AGNs of moderate radio luminosity ($L_{1.4\text{ GHz}} = 10^{23} - 10^{25} \text{ W Hz}^{-1}$) having the broadest [O III] $\lambda 5007$ profiles. Conversely, we find only a modest change in the [O III] $\lambda 5007$ profile with increasing radio loudness and find no significant difference between the [O III] $\lambda 5007$ profiles of broad- and narrow-line Seyfert 1s. When binned according to Eddington ratio, only the AGNs in our highest bin (i.e. > 0.3) show any signs of having broadened [O III] $\lambda 5007$ profiles, although the small numbers of such extreme AGNs in our sample mean we cannot rule out that other processes (e.g. radio jets) are responsible for this broadening. The [O III] $\lambda 5007$ profiles of type 1 and type 2 AGNs show the same trends in terms of line width, but type 1 AGNs display a much stronger ‘blue wing’, which we interpret as evidence of outflowing ionized gas. We perform multicomponent fitting to the H β , [O III] $\lambda\lambda 4959, 5007$, [N II] $\lambda\lambda 6548, 6584$ and H α lines for all the AGNs in our sample to calculate the proportions of AGNs with broad [O III] $\lambda 5007$ profiles. The individual fits confirm the results from our stacked spectra; AGNs with $L_{1.4\text{ GHz}} > 10^{23} \text{ W Hz}^{-1}$ are roughly five times more likely to have extremely broad [O III] $\lambda 5007$ lines (full width at half-maximum, $\text{FWHM}_{\text{Avg}} > 1000 \text{ km s}^{-1}$) compared to lower $L_{1.4\text{ GHz}}$ AGNs, and the width of the [O III] $\lambda 5007$ line peaks in moderate-radio-luminosity AGNs ($L_{1.4\text{ GHz}} \sim 10^{24} \text{ W Hz}^{-1}$). Our results are consistent with the most disturbed gas kinematics being induced by compact radio cores (rather than powerful radio jets), although broadened [O III] $\lambda 5007$ lines are also present, but much rarer, in low- $L_{1.4\text{ GHz}}$ systems. Our catalogue of multicomponent fits is freely available as an online resource for statistical studies of the kinematics and luminosities of the narrow- and broad-line AGN regions and the identification of potential targets for follow-up observations at <http://sites.google.com/site/sdssalpaka>.

Key words: catalogues – ISM: kinematics and dynamics – galaxies: active – quasars: emission lines – radio continuum: galaxies.

1 INTRODUCTION

The most successful models of galaxy evolution invoke interactions between accreting supermassive black holes (hereafter SMBHs) and their host galaxies to reproduce the most fundamental properties of

★ E-mail: j.r.mullaney@dur.ac.uk

today's galaxy population (e.g. Di Matteo, Springel & Hernquist 2005; Bower et al. 2006). Many of these models assume that a fraction of the energy released by an accreting SMBH (i.e. an active galactic nucleus; hereafter AGN) drives gas and dust from the central regions of a galaxy, quenching star formation (e.g. Di Matteo et al. 2005; Springel, Di Matteo & Hernquist 2005; Hopkins et al. 2006).¹ However, it is not yet clear what process drives these galaxy-scale 'outflows', with both radio jets (either compact or extended; e.g. Nesvadba et al. 2006, 2008; Rosario et al. 2010) and radiation pressure (e.g. Alexander et al. 2010) having been suggested as viable mechanisms.

Most observational evidence for galaxy-scale outflows has so far been based on pointed observations of a handful of objects (e.g. Nesvadba et al. 2006, 2008; Alexander et al. 2010; Rosario et al. 2010; Greene et al. 2011; Harrison et al. 2012). These studies, while providing considerable insight into the scale and detailed kinematics of the outflows, are subject to strong selection biases (e.g. pre-selected for radio loudness/luminosity, bolometric luminosity, unique emission-line properties). Therefore, it has so far been difficult to place these outflows in the context of the general AGN and galaxy populations and establish which AGN properties are most conducive to their production (i.e. radio jets/cores, high bolometric luminosity, high Eddington ratio, etc.). In this study, we aim to address this by taking the complementary approach of exploring in coarser detail the gas kinematics of much larger numbers of AGNs with physical properties spanning large sections of parameter space.

The primary diagnostics that the above studies used to initially identify kpc-scale outflows were broad, often blueshifted [O III] $\lambda 5007$ emission lines in integrated (i.e. 1D) rest-frame optical spectra. Since [O III] $\lambda 5007$ is produced through a forbidden transition, it is only emitted by low-density gas. As such, any broadening or shifting of the [O III] $\lambda 5007$ emission lines is the result of strong velocity gradients or bulk motions (i.e. disturbed kinematics) in the so-called narrow-line region (hereafter NLR) of AGNs which can be extended over kpc scales (e.g. Pogge 1989), as opposed to the dense, sub-pc-sized broad-line region.

While broadened (beyond that expected from galaxy rotation) and asymmetric [O III] $\lambda 5007$ profiles in AGN spectra have been reported for over three decades (early studies include, e.g., Heckman et al. 1981; Feldman et al. 1982; Heckman, Miley & Green 1984; Whittle 1985a), there remains some uncertainty as to which physical process causes the gas kinematics that result in these profiles. Early studies of small to moderately sized samples of nearby AGNs (numbering <150) reported positive correlations between [O III] $\lambda 5007$ profile widths and both [O III] $\lambda 5007$ and 1.4 GHz radio luminosities for flat-spectrum radio sources with $L_{1.4\text{GHz}} < 3 \times 10^{24} \text{ W Hz}^{-1}$ (e.g. Heckman et al. 1984, also Wilson & Willis 1980; Whittle 1985b). However, since $L_{[\text{O III}]}$ is broadly correlated with $L_{1.4\text{GHz}}$ (e.g. Baum & Heckman 1989; Rawlings et al. 1989; Zirbel & Baum 1995; Tadhunter et al. 1998; Wills et al. 2004; de Vries et al. 2007), these early studies were unable to determine which of these parameters were more fundamentally linked to the kinematics of the NLR. With the availability of large spectroscopic data sets (e.g. the SDSS and 2dF surveys), more recent studies have explored how the [O III] $\lambda 5007$ profile changes across wide areas of parameter space. For example, using a sample

of 1749 SDSS-selected AGNs, Greene & Ho (2005a) found that the narrow 'core' of the [O III] $\lambda 5007$ line traced the kinematics of the host galaxy, with any departures correlating with the Eddington ratio of the AGN (also Bian et al. 2006; although see also Zhang et al. 2011). However, while some recent studies have explored, in detail, the links between gas kinematics and the radio properties for small samples of AGNs (e.g. Wu 2009; Husemann et al. 2013), an analysis of much larger samples is needed to break the degeneracy between radio and [O III] $\lambda 5007$ luminosities to determine how gas kinematics relate to the radio properties for the AGN population in general.

In this study, we use the SDSS spectral data base to derive the average [O III] $\lambda 5007$ line profiles of a large sample (i.e. numbering 24 267) of optically selected AGNs at $z < 0.4$ and explore how these average profiles change as a function of key AGN parameters [specifically, [O III] $\lambda 5007$ luminosity, Eddington ratio, radio loudness, radio luminosity and spectral classification (i.e. optical type 1, type 2)]. While the single-aperture spectra provided by the SDSS provide no information regarding the extent of any kinematically disturbed gas, the SDSS spectral archive provides the statistics needed to determine how gas kinematics relate to other AGN properties (including the radio properties) and establish the prevalence of high gas velocities among different AGN subpopulations. Furthermore, it is important to stress that the redshift range of our sample does not span the epoch of peak star formation and AGN activity (i.e. $z \sim 1-3$; Merloni, Rudnick & Di Matteo 2004; Hopkins & Beacom 2006; Aird et al. 2010) when quasar-mode AGN-driven outflows are thought to have had their greatest impact on galaxy growth. However, the high signal-to-noise ratios (S/N) and large statistics allowed by surveys of the local Universe can give us a better insight into which physical processes are most capable of disturbing the gas reservoirs around an AGN.

In the following section, we outline our initial source selection procedure, describe our multicomponent line fitting routine and outline how the results from this routine were used to reclassify and analyse the AGNs in our sample. In Section 3, we describe the results derived from the average [O III] $\lambda 5007$ profiles, paying particular attention to how the [O III] $\lambda 5007$ profile changes as a function of the parameters outlined above. In Section 4, we present the results from our multicomponent fitting routine and calculate the fractions of local, optically selected AGNs that show broad [O III] $\lambda 5007$ lines. We discuss the implications of our main results in Section 5 and summarize our findings in Section 6. We adopt $H_0 = 71 \text{ km s}^{-1} \text{ Mpc}^{-1}$, $\Omega_M = 0.27$ and $\Omega_\Lambda = 0.73$ throughout.

2 SAMPLE SELECTION, CLASSIFICATION AND ANALYSIS

The large number of flux-calibrated galaxy and AGN spectra contained within the SDSS make it an ideal resource for deriving the average [O III] $\lambda 5007$ profiles of optically selected AGNs and quantifying the proportions of the AGN subpopulation that display broad [O III] $\lambda 5007$ profiles. However, careful source selection is necessary to remove contaminants such as H II galaxies from our sample of SDSS AGNs. We start this section with a description of how we used the results from the SDSS spectral fitting routine to efficiently remove those sources whose optical emission lines are least likely to be the result of AGN-dominated ionization processes [e.g. H II, low-ionization nuclear emission-line regions (LINERs), etc.]. We then describe how we used the results of our own emission-line fitting routine to: (a) further refine our AGN sample, removing any remaining contaminants in the process and (b) measure any broad

¹ This 'quasar-mode' feedback is distinct from the 'radio-mode', in which the intracluster medium is prevented from cooling on to galaxies (where it can form stars) by powerful, extended, radio jets produced by a low-accretion-rate, radio-loud AGN.

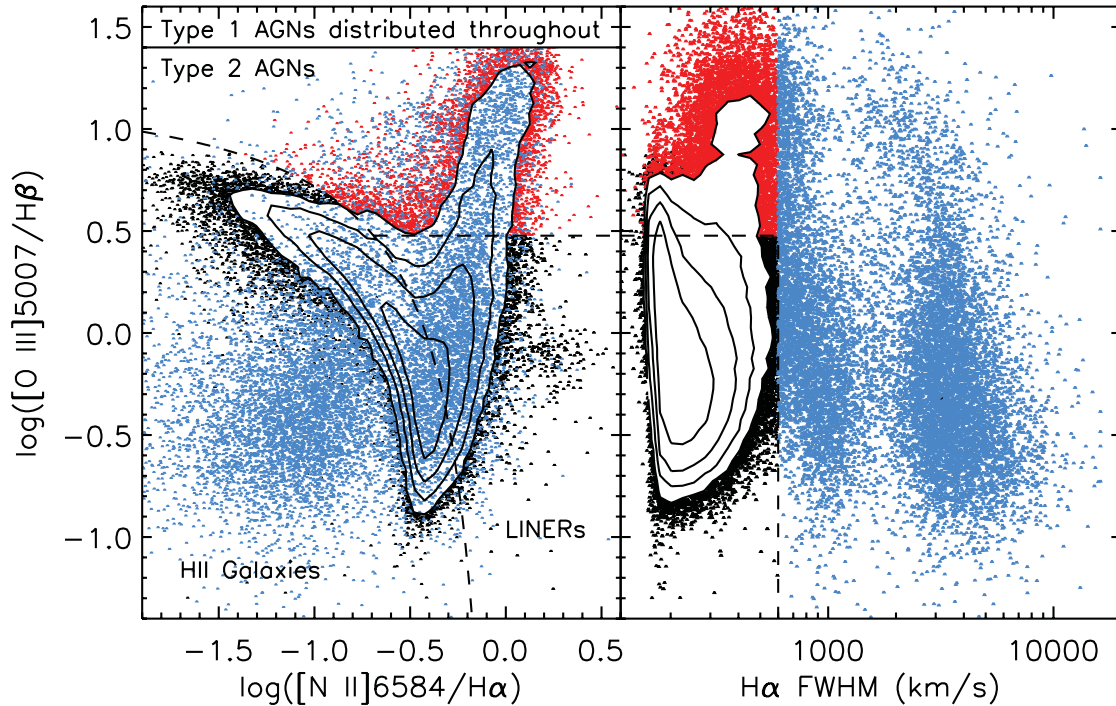


Figure 1. Plots highlighting the line ratio and $\text{FWHM}_{\text{H}\alpha}$ cuts used to identify candidate type 1 and type 2 AGNs (shown as blue and red points, respectively; black points are used to indicate LINERs and H II galaxies) in the SDSS parent sample of emission-line galaxies. All values used to create both these plots were taken directly from the SDSS data base. Left: $[\text{O III}] \lambda 5007/\text{H}\beta$ versus $[\text{N II}] \lambda 6584/\text{H}\alpha$ BPT diagram of all galaxies in the parent sample. The dashed lines indicate the criteria used to discriminate between candidate narrow-line objects [i.e. type 2 AGNs, LINERs and H II galaxies; discrimination lines taken from Ho, Filippenko & Sargent (1997) and Kauffmann et al. (2003)]. Right: $[\text{O III}] \lambda 5007/\text{H}\beta$ versus $\text{FWHM}_{\text{H}\alpha}$ of the same sources. The width of the $\text{H}\alpha$ line was used to discriminate between narrow-line galaxies (i.e. candidate type 2 AGNs, LINERs and H II galaxies) and candidate ‘broad-line’ (type 1) AGNs. A conservative $\text{FWHM}_{\text{H}\alpha} > 600 \text{ km s}^{-1}$ cut was used to identify candidate type 1 AGNs. We note that the bimodal distribution of $\text{FWHM}_{\text{H}\alpha}$ (a result of an apparent dearth of AGNs around $\text{H}\alpha = 2000 \text{ km s}^{-1}$) is a feature produced by the SDSS spectral fitting routine. This bimodality disappears when the $\text{H}\alpha$ profiles are fitted with multiple components (see Section 2.3). Contours are used in both plots to show regions of very high densities of narrow-line galaxies (i.e. type 2 AGNs, LINERs and H II galaxies).

emission-line components likely missed by the single-component fits carried out by the SDSS emission-line fitting routine. Next, we explain how we used the FIRST (White et al. 1997) and NVSS (Condon et al. 1998) radio coverage of the SDSS field to identify the radio-loud/luminous AGNs in our SDSS sample, allowing us to explore the potential role of radio AGNs in driving outflows. Finally, we describe our spectral stacking procedure which we use as our principal form of analyses.

2.1 SDSS query

As the main focus of this study is to determine how the profile of the $[\text{O III}] \lambda 5007$ emission line relates to other key AGN properties, we selected all extragalactic spectroscopic sources in the SDSS-DR7 catalogue (Abazajian et al. 2009) with $[\text{O III}] \lambda 5007$ detected in emission (at $>3\sigma$) by the SDSS spectral fitting routine. Since we rely on emission-line diagnostics to identify AGNs (see Section 2.2), we required that the $\text{H}\alpha$, $\text{H}\beta$ and $[\text{N II}] \lambda 6584$ lines are also detected in emission (again, at $>3\sigma$ confidence). In ensuring that the $[\text{N II}] \lambda 6584$ line is detected, sources at redshifts $z > 0.4$ (at which point $[\text{N II}] \lambda 6584$ is shifted out of the wavelength coverage of the SDSS spectra) are, by default, excluded from the sample. This query returned 239 083 SDSS targets.

2.2 Selection of AGNs

The vast majority of extragalactic emission-line sources in the SDSS data base are dominated by star formation rather than AGN activity

and need to be removed from the sample prior to further analysis. We used a combination of emission-line flux ratios (‘BPT’ diagnostics; Baldwin, Phillips & Terlevich 1981) and line widths (as measured by the SDSS spectral fitting routine) to remove the ~ 90 per cent of the initial sample likely dominated by star formation. We classified all narrow-line objects (defined here as having full width at half-maximum $\text{FWHM}_{\text{H}\alpha} < 600 \text{ km s}^{-1}$) as being probable type 2 AGNs if their $[\text{O III}] \lambda 5007/\text{H}\beta$ and $[\text{N II}] \lambda 6584/\text{H}\alpha$ flux ratios satisfy the diagnostics outlined in Kauffmann et al. (2003; see our Fig. 1) and identify all sources with $\text{FWHM}_{\text{H}\alpha} > 600 \text{ km s}^{-1}$ as *potential* type 1 AGNs.² Our choice of $\text{FWHM}_{\text{H}\alpha}$ cut is a compromise between obtaining as complete a sample of type 1 AGNs as possible and the exclusion of H II galaxies and LINERs, whose numbers increase significantly at $\text{FWHM}_{\text{H}\alpha} < 600 \text{ km s}^{-1}$. Tests of a 10 per cent sampling of these H II and LINERs using our multicomponent fitting routine (see Section 2.3 and Appendix A) suggest an ≈ 0.3 per cent type 1 AGN contamination amongst these non-AGNs. As such, we estimate that we are missing ~ 700 type 1 AGNs by excluding H II and LINERs from further analysis. These ‘unidentified’ type 1 AGNs will be the focus of a later study.

The above cuts identified 25 670 potential type 1 and type 2 AGNs that were passed to our multicomponent fitting routine for further

² We rely on the FWHM of the $\text{H}\alpha$ line, rather than $\text{H}\beta$, to ensure that we include intermediate-class AGNs (e.g. type 1.8, 1.9, etc.) in our type 1 classification.

analysis and possible reclassification. The remaining 213 413 galaxies are excluded from any further analysis.

2.3 Multicomponent fitting routine

In the previous subsection we described how we used the results from the SDSS emission-line fitting routine to crudely select samples of type 1 and type 2 AGNs in the SDSS data base. However, the single-Gaussian (i.e. one per emission line) fits performed by the SDSS pipeline cannot account for the complex emission-line profiles that are common among AGN spectra. Instead, we developed our own multicomponent fitting routine to accurately measure these line profiles. We used this routine to re-measure the profiles of the $H\alpha$, $H\beta$, $[N II] \lambda 6548, 6584$ and $[O III] \lambda 5007$ emission lines in all 25 670 spectra identified in Section 2.2. The results from this multicomponent fitting routine were used to (a) obtain more robust AGN classifications and (b) identify any broadening or shifting of the $[O III] \lambda 5007$ emission line. A detailed description of our multicomponent fitting routine is given in Appendix A. To summarize, up to two Gaussians are fitted to each of the forbidden $[O III] \lambda 4959$, $[O III] \lambda 5007$, $[N II] \lambda 6548$ and $[N II] \lambda 6584$ emission lines (to account for any line asymmetries and/or broad components) and up to three Gaussians to each of the permitted $H\alpha$ and $H\beta$ lines (up to two Gaussians to account for the narrow component of these permitted lines and one Gaussian to account for the broad component in the case of type 1 AGNs). The two Gaussians used to model the narrow component of these permitted lines are fixed to have the same profile as the forbidden $[O III]$ and $[N II]$ lines.

2.4 Source classification

We used the results from our multicomponent line fitting routine to refine the classifications of the AGNs in our sample beyond that which is capable using the single-component fits performed by the standard SDSS pipeline. In what follows, we outline how we separated our sample into broad- and narrow-line Seyfert 1s (hereafter BLS1s, NLS1s, respectively, and referred to collectively as type 1 AGNs), type 2 AGNs and those sources that, following an analysis with our multicomponent fitting routine, were identified as being non-AGN dominated (and excluded from further consideration).

2.4.1 Type 1 AGNs (BLS1s and NLS1s)

For each source we used the FWHM of the broadest $H\alpha$ component to identify type 1 AGNs and distinguish between BLS1s and NLS1s. By using $H\alpha$ rather than $H\beta$ as the discriminator, we will avoid classifying intermediate-type AGNs (e.g. 1.8, 1.9; Osterbrock 1981) as NLS1s since, by definition, intermediate types show evidence of a broad component in the $H\alpha$ line (but not necessarily in the $H\beta$ line). A source was classified as a type 1 AGN if an extra Gaussian (i.e. beyond that needed to fit the forbidden lines) provided a significantly better fit (at >99 per cent confidence) to the $H\alpha$ line, and that Gaussian constitutes at least 50 per cent of the total emission-line flux and has $FWHM_{H\alpha} > 600 \text{ km s}^{-1}$ (10 548 sources). The >50 per cent cut excludes 995 AGNs that our fitting routine measures $FWHM_{H\alpha} > 600 \text{ km s}^{-1}$, 717 (i.e. ~ 72 per cent) of which are subsequently classified as type 2 AGNs. These 995 AGNs represent <10 per cent of either type 1s or type 2s and, subsequently, their reclassification has little impact on our results yet ensures that we only include genuine type 1 AGNs in that group.

As per the classical, yet arbitrary, definition of Goodrich (1989), all of those type 1 AGNs whose broadest $H\alpha$ component has an $FWHM_{H\alpha} > 2000 \text{ km s}^{-1}$ were subclassified as BLS1s (9455 sources). The remaining type 1 AGNs (1093 sources) were classed as NLS1s (of which 1024, or ~ 93 per cent, have broad $H\alpha$ components that satisfy $1000 < FWHM_{H\alpha} < 2000 \text{ km s}^{-1}$).

2.4.2 Type 2 AGNs

We used the Kauffmann et al. (2003) emission-line (BPT) diagnostics to identify type 2 AGNs in the remaining sample (i.e. those that have not already been identified as type 1 AGNs). Where two Gaussians are fitted to the $[O III] \lambda 4959, 5007$ and $[N II] \lambda 6548, 6584$ lines, we use the combined flux of these components. In such cases, we use the combined flux of the two narrow components of the $H\beta$ and $H\alpha$ lines. Similarly, when only one Gaussian is needed to fit the $[O III] \lambda 4959, 5007$ and $[N II] \lambda 6548, 6584$ lines, we only use the flux of the single narrowest Gaussian of the $H\alpha$ and $H\beta$ lines (i.e. if present, we always exclude any $H\alpha$ and $H\beta$ broad components when calculating their narrow-line flux). In this way, we classify 13 716 type 2 AGNs.

2.4.3 Non-AGN Dominated

Any narrow-line objects (i.e. non-type 1 AGNs) which, after being analysed by our multicomponent fitting routine, were not classified as type 2 AGNs were removed from the sample (1406 sources), leaving 24 264 confirmed AGNs (of either type 1 or type 2). After analyses with our emission-line fitting routine, these rejected sources were found to predominantly lie in the LINER of the BPT diagram and have $FWHM_{H\alpha} > 600 \text{ km s}^{-1}$ as measured by the SDSS pipeline.

2.5 1.4 GHz radio coverage

One of the key aims of this study is to determine how the kinematics of the $[O III] \lambda 5007$ emitting gas relates to the radio properties of the AGN. To quantify the radio properties of our sample, we performed a three-way cross-matching between our optical (SDSS) catalogue and the NVSS and FIRST radio catalogues, largely following the procedure outlined in Best et al. (2005). As such, we only use radio fluxes from the NVSS catalogue, but use the higher spatial resolution information provided by the FIRST survey to ensure a low level of contamination within our optical–radio matched catalogue. Contrary to Best et al. (2005), the goal of this study is not to obtain a highly complete sample of radio sources, but instead to measure the radio properties of optically selected AGNs. As such, we considered all NVSS sources with 1.4 GHz fluxes $>2 \text{ mJy}$; this lower limit is a factor of 2.5 below that used by Best et al. (2005). However, we note that the integrated 1.4 GHz flux densities of all the sources in our catalogue have $S/N > 3$. For those sources not detected by the NVSS, we assumed an integrated 1.4 GHz flux density upper limit of 2 mJy.

Of the 10 548 type 1 and 13 716 type 2 AGNs in our SDSS sample, 535 (i.e. ~ 5 per cent) and 1453 (i.e. ~ 11 per cent), respectively, are found to have radio counterparts (representing ~ 8 per cent of all AGNs in our sample). The discrepancy between the fraction of type 1 AGNs with radio detections and that of type 2 is likely to be due to the redshift distributions of these classes of galaxies in our sample. Since they are brighter at optical wavelengths, type 1 AGNs are more likely to satisfy the apparent magnitude cut for a spectral

follow-up by the SDSS. The higher average redshift of the type 1 AGNs means a smaller fraction of them are detected in the NVSS radio survey (which has roughly a constant flux limit).

We assume a radio spectral index of $\alpha = 0.8$ when calculating the rest-frame 1.4 GHz radio luminosity, where $F_\nu \propto \nu^{-\alpha}$ (Ibar et al. 2010).

2.6 Spectral stacks and average [O III] $\lambda 5007$ profiles

In addition to our fits to individual spectra, we also rely heavily on spectral stacking to derive the average [O III] $\lambda 5007$ profiles of optically selected AGNs. By binning the AGN sample in terms of luminosity, Eddington ratio and radio properties, we can use these stacks to isolate general trends in the [O III] $\lambda 5007$ profile with respect to these parameters. The benefit of spectral stacking is that it is less susceptible to systematic biases than results derived solely from individual fits (e.g. the low S/N of fainter AGNs affecting our ability to detect broadened line components) and, by considering relative changes in the average profile of the [O III] $\lambda 5007$ line, to measures of the systematic velocity of the AGN. In Section 4, we use the results from our spectral stacks to motivate further analyses using the individual AGN spectra.

The spectral stacks were built by coadding the continuum-subtracted spectra provided by the SDSS data base. Each spectrum was shifted into the rest frame using the [O III] $\lambda 5007$ redshift derived from our fits (assuming that the narrowest [O III] $\lambda 5007$ component lies at the systematic redshift). We note that the redshift derived from the [O III] $\lambda 5007$ line is in very good agreement with the redshift provided by the SDSS data base – a Gaussian fit to the $\Delta z = z_{\text{SDSS}} - z_{[\text{O III}]}$ distribution reveals an average offset of $\Delta z = (0.9 \pm 2.1) \times 10^{-4}$ (i.e. $26 \pm 63 \text{ km s}^{-1}$); indeed, our tests show that there is no significant impact on our results if we adopt the SDSS-reported redshifts instead. We take a bootstrapping approach to calculate the error on the average emission-line profiles. We select, at random, a third of the sample in each of our bins and stack their spectra. We repeat this process 1000 times and calculate the standard deviation at each wavelength of the resulting distribution of stacked spectra. This standard deviation is then adopted as the error on the stacked line profiles.

When stacking as a function of radio properties (i.e. $L_{1.4 \text{ GHz}}$ and R_{Rad}), we only include radio-undetected sources when (a) their upper limits are consistent with the upper boundary of the bin and (b) there is no lower boundary on the bin (e.g. $L_{1.4 \text{ GHz}} < 10^{22} \text{ W Hz}^{-1}$ and $R_{\text{Rad}} < 10^{-1}$).

3 RESULTS FROM SPECTRAL STACKING

In our analyses we explore the kinematics of the AGNs' NLRs as portrayed by the profiles of the forbidden [O III] $\lambda 5007$ emission lines. Using stacked spectra, we search for general trends in the profiles of the [O III] $\lambda 5007$ lines with respect to various key AGN parameters (specifically, bolometric luminosity, Eddington ratio, radio loudness, radio luminosity and AGN orientation). In Section 4 we use the results from the emission-line fitting routine described in Section 2.3 (see also Appendix A) to estimate the proportions of optically selected AGNs that have either very broad or highly shifted [O III] $\lambda 5007$ lines or components.

We initially focus our analyses on type 1 AGNs. Assuming that outflows are driven radially outwards perpendicular to the plane of the dusty torus/accretion disc, then from AGN unification models (e.g. Antonucci 1993) any outflowing material driven by the AGN

(either by jets or radiatively driven winds) should show a stronger blueshift (asymmetry) in the spectra of type 1 AGNs (compared to type 2s) as the outflow will be directed more along our line of sight. As such, if the AGNs are indeed driving outflows, and these outflows emit [O III] $\lambda 5007$, we should expect type 1 AGNs to show stronger [O III] $\lambda 5007$ line shifts. In Section 3.3, we compare the results derived from our type 1 population with the type 2 AGNs in our sample to explore the influence of AGN orientation on the observed emission-line profiles and measured gas kinematics.

3.1 The average [O III] $\lambda 5007$ profile of type 1 AGNs

In Fig. 2, we present the average [O III] $\lambda 5007$ profile derived from stacking all type 1 AGNs in our sample. This profile displays a prominent blue wing and is well fitted using two Gaussian components, a narrow (i.e. $\text{FWHM} = 335 \text{ km s}^{-1}$) component and a broader (i.e. $\text{FWHM} = 851 \text{ km s}^{-1}$) component that is blueshifted by 148 km s^{-1} with respect to the narrow component. The flux contained within the broader component represents ≈ 45 per cent of the total line flux.

In the following subsection, we consider whether the profile of the [O III] $\lambda 5007$ line changes as a function of bolometric luminosity (L_{AGN}), Eddington ratio (λ_{Edd}), radio loudness (R_{Rad}), radio luminosity ($L_{1.4 \text{ GHz}}$) and orientation. We do this by binning the sample in terms of these properties and use spectral stacking to derive the average [O III] $\lambda 5007$ emission-line profiles of the AGNs in each bin.

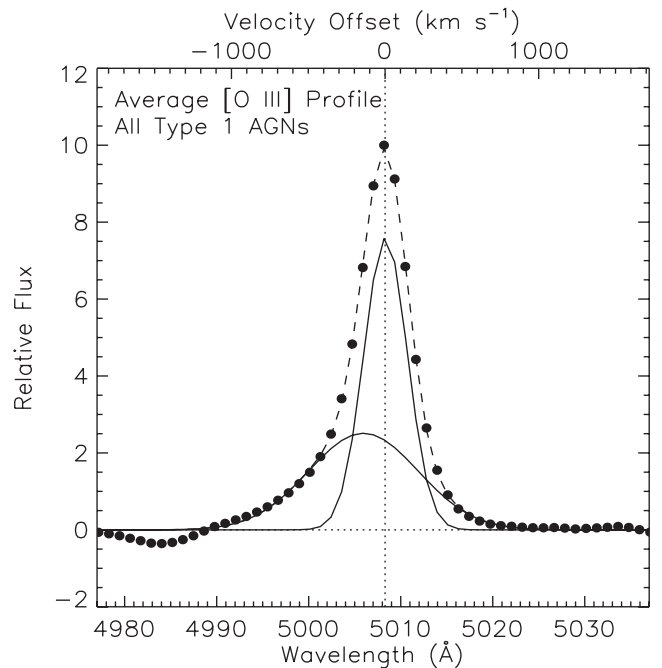


Figure 2. Average [O III] $\lambda 5007$ profile of type 1 AGNs in our sample derived from spectral stacking. This profile shows a strong blue wing (blueward asymmetry) that is well modelled by a broad (i.e. $\text{FWHM} = 851 \text{ km s}^{-1}$) second Gaussian component that is offset from the narrower component (i.e. $\text{FWHM} = 335 \text{ km s}^{-1}$) by 148 km s^{-1} . The fit produced by combining these two components is shown by the dashed line.

3.2 Correlations between the average [O III] $\lambda 5007$ profile and key AGN properties

3.2.1 [O III] $\lambda 5007$ luminosity

If outflows from AGNs are driven by radiative forces, and these outflows manifest themselves as blueshifted [O III] $\lambda 5007$ wings, then we may expect the observed properties of these wings to change as a function of the AGN luminosity. The [O III] $\lambda 5007$ luminosity (hereafter $L_{[\text{O III}]}$) is thought to be a proxy measure of the bolometric AGN luminosity (e.g. Maiolino & Rieke 1995; Bassani et al. 1999; Risaliti, Maiolino & Salvati 1999; Heckman et al. 2005), so here we investigate the relationship between [O III] $\lambda 5007$ profile and $L_{[\text{O III}]}$.

In the top-left panel of Fig. 3 we present the average [O III] $\lambda 5007$ profiles of type 1 AGNs in our sample divided into bins of $\log(L_{[\text{O III}]})$, with bin intervals of $\Delta \log(L_{[\text{O III}]}) = 1$ over $L_{[\text{O III}]} = 10^{40} - 10^{44} \text{ erg s}^{-1}$. We calculate $L_{[\text{O III}]}$ using the results from our multicomponent fitting routine, assuming the redshift calculated from the [O III] $\lambda 5007$ line; when two [O III] $\lambda 5007$ components are present, $L_{[\text{O III}]}$ is the combined luminosity of both components, although we note that our results remain unchanged when only the luminosity of the narrow [O III] $\lambda 5007$ component is used. We use the Balmer decrement (using the ratio of the narrow H α and H β components calculated from our fits) and assume the Cardelli, Clayton & Mathis (1989) reddening curve to correct for the effects of reddening on $L_{[\text{O III}]}$.

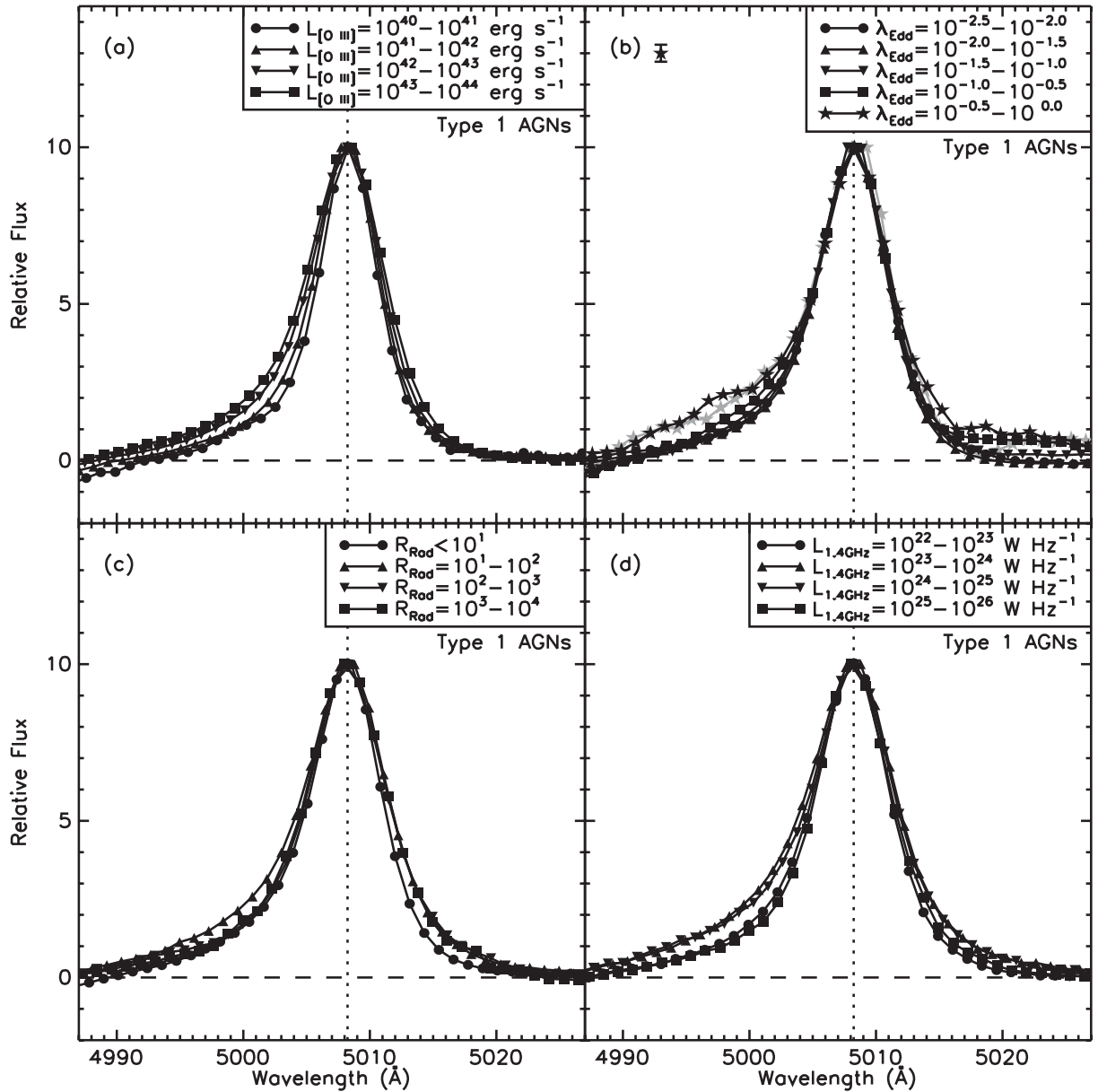


Figure 3. Average [O III] $\lambda 5007$ profiles of type 1 AGNs binned according to (a) [O III] luminosity, (b) Eddington ratio, (c) radio loudness and (d) radio luminosity. The grey curve in plot (b) shows the average profile of the highest Eddington ratio AGNs after excluding those spectra that show prominent Fe II emission that can contaminate [O III] $\lambda 5007$. For presentation purposes we do not show the errors on the stacked profiles which, with the exception of the highest Eddington ratio bin in panel (b) (see representative error bar), are smaller than the points.

Table 1. Sample properties after accounting for the correlation between $L_{[\text{O III}]}$ and $L_{1.4\text{ GHz}}$.

L_{Rad} (1)	$L_{[\text{O III}]}$ (2)	N (3)	Med. L_{Rad} (4)	Med. $L_{[\text{O III}]}$ (5)
$<10^{23}$	$10^{40}-10^{41}$	129	<23	40.8
$<10^{23}$	$10^{41}-10^{42}$	129	<23	41.6
$<10^{23}$	$10^{42}-10^{43}$	129	<23	42.3
$>10^{23}$	$10^{41}-10^{42}$	64	24.1	41.7
$>10^{23}$	$10^{42}-10^{43}$	77	24.0	42.5
$>10^{23}$	$10^{43}-10^{44}$	77	24.1	43.3
$<10^{22}$	$<10^{42}$	33	<22	41.5
$10^{22}-10^{23}$	$<10^{42}$	33	22.6	41.7
$10^{23}-10^{24}$	$<10^{42}$	32	23.4	41.8
$10^{24}-10^{25}$	$<10^{42}$	33	24.3	41.7
$<10^{22}$	$>10^{42}$	39	<22	42.1
$10^{22}-10^{23}$	$>10^{42}$	42	22.7	42.3
$10^{23}-10^{24}$	$>10^{42}$	42	23.5	42.4
$10^{24}-10^{25}$	$>10^{42}$	42	24.3	42.4
$10^{25}-10^{26}$	$>10^{42}$	37	25.5	42.4

Notes. The first six rows show the samples that have been selected to have roughly constant $L_{1.4\text{ GHz}}$ but increasing $L_{[\text{O III}]}$. The lower nine rows show those samples that have been selected such that $L_{[\text{O III}]}$ remains roughly constant, but $L_{1.4\text{ GHz}}$ increases. (1) Range of $L_{1.4\text{ GHz}}$; (2) range of $L_{[\text{O III}]}$; (3) the number of sources in each subsample; (4) the median radio luminosity; (5) the median $[\text{O III}] \lambda 5007$.

The stacked $[\text{O III}] \lambda 5007$ emission-line profiles of type 1 AGNs display increasingly prominent blue wings with increasing $L_{[\text{O III}]}$. However, before interpreting this result as evidence that radiative forces are largely responsible for the kinematics of the $[\text{O III}] \lambda 5007$ emitting gas, it is important to account for the known positive correlation between $L_{[\text{O III}]}$ and AGN radio power (e.g. Baum & Heckman 1989; Rawlings et al. 1989; Zirbel & Baum 1995; Tadhunter et al. 1998; Wills et al. 2004; de Vries et al. 2007). For this, we perform the same experiment as described above (i.e. stacking as a function of $L_{[\text{O III}]}$) however this time controlling for radio luminosity to ensure that the median radio luminosities of the stacks are consistent to within a factor of 3 with each other (see Table 1). We have also attempted to keep the number of sources in each stack roughly the same by randomly selecting, without replacement, sources from each bin. The numbers in each stack are therefore constrained by two effects: (i) the number of sources in the bin containing the smallest number of AGNs and (ii) the ability to select sources from each bin with radio luminosities that are consistent to within a factor of 3. The combination of these two effects is why the numbers of stacked sources are not *exactly* the same in each of the bins.

The results of this experiment are shown in the top two panels of Fig. 4. Here, we have divided the sample into radio weak (i.e. $L_{1.4\text{ GHz}} < 10^{23} \text{ W Hz}^{-1}$, including any upper limits that also satisfy this criterion; panel a) and radio powerful (i.e. $L_{1.4\text{ GHz}} > 10^{23} \text{ W Hz}^{-1}$, excluding all upper limits; panel b). When the stacks are controlled for radio luminosity, the change in average $[\text{O III}] \lambda 5007$ profile as a function of $L_{[\text{O III}]}$ is much less pronounced in both the radio weak and radio strong samples.³ We do note, however, that

³ We note that we do not calculate the average profile for the highest $L_{[\text{O III}]}$ bin (i.e. $L_{[\text{O III}]} = 10^{43}-10^{44} \text{ erg s}^{-1}$) of the radio weak AGNs, nor the lowest $L_{[\text{O III}]}$ bin (i.e. $L_{[\text{O III}]} = 10^{40}-10^{41} \text{ erg s}^{-1}$) of the radio strong AGNs, as there are too few sources to provide reliable averages – a consequence of the correlation between $L_{[\text{O III}]}$ and radio power.

a slight increase in the prominence of the $[\text{O III}] \lambda 5007$ blue wings with increasing $L_{[\text{O III}]}$ still remains in both the radio strong and weak subsamples. However, comparing the top two panels of Fig. 4 reveals a striking difference in the average profiles of radio weak and radio strong AGNs, with all the radio strong stacks having broader $[\text{O III}] \lambda 5007$ profiles than their equivalent radio weak stack. We explore this further in Section 3.2.3.

3.2.2 Eddington ratio

Previous studies of the $[\text{O III}] \lambda 5007$ line profile have concluded that the Eddington ratio (i.e. $\lambda_{\text{Edd}} = L_{\text{AGN}}/L_{\text{Edd}}$, where L_{Edd} is the Eddington luminosity of the central SMBH) of the AGN plays a key role in dictating both the FWHM and blueshift of the $[\text{O III}] \lambda 5007$ line, including whether it displays a strong blue wing (e.g. Greene & Ho 2005a). Here, we consider whether our analyses confirm that the $[\text{O III}] \lambda 5007$ profile is correlated with the Eddington ratio of the AGN.

To estimate the Eddington luminosity of the AGN, we use the SMBH mass calculated from the FWHM and luminosity of the $\text{H}\alpha$ emission line (see equation 6 of Greene & Ho 2005b). We only calculate L_{Edd} for type 1 AGNs and use only the FWHM of the broadest $\text{H}\alpha$ Gaussian. Here, the bolometric luminosity (i.e. L_{AGN}) is estimated from the luminosity of the $\text{H}\alpha$ line using a combination of the $L_{\text{H}\alpha} - L_{5100}$ and $L_{5100} - L_{\text{AGN}}$ correction factors described in Greene & Ho (2005a) and Netzer & Trakhtenbrot (2007), respectively. These combine to give an expression for the Eddington ratio of

$$\lambda_{\text{Edd}} = \frac{L_{\text{AGN}}}{L_{\text{Edd}}} \approx 0.43 f_{10} \left(\frac{L_{\text{H}\alpha}}{10^{42} \text{ erg s}^{-1}} \right)^{0.31} \left(\frac{\text{FWHM}_{\text{H}\alpha}}{10^3 \text{ km s}^{-1}} \right)^{-2}, \quad (1)$$

where f_{10} is the dimensionless $L_{5100} - L_{\text{AGN}}$ bolometric correction factor (see Netzer & Trakhtenbrot 2007) in units of 10. We assume $f_{10} = 1$ throughout, although note that this has no effect on our final results as we are only concerned with relative changes in the $[\text{O III}] \lambda 5007$ profile.

The average profiles of the type 1 AGNs in our sample, stacked in terms of λ_{Edd} , are presented in the top-right panel of Fig. 3. We find no significant difference in the average $[\text{O III}] \lambda 5007$ profiles over the range $\lambda_{\text{Edd}} = 3 \times 10^{-3} - 3 \times 10^{-2}$, while the $[\text{O III}] \lambda 5007$ profiles of $\lambda_{\text{Edd}} = 3 \times 10^{-2} - 1$ AGNs display increasingly prominent blue wings with increasing λ_{Edd} . The average spectrum of AGNs in the highest λ_{Edd} bin that we consider (i.e. $\lambda_{\text{Edd}} = 0.3 - 1$) shows evidence of contamination from Fe II (beyond, e.g. $\sim 5020 \text{ \AA}$) that could alter the apparent profile of the $[\text{O III}] \lambda 5007$ line.⁴ When we remove those AGNs in the highest λ_{Edd} bin that show evidence of having strong Fe II emission at other wavelengths in their spectrum, the resulting stacked $[\text{O III}] \lambda 5007$ profile remains largely unchanged. As with our stacks as a function of $L_{[\text{O III}]}$, we must use caution before directly associating this broadening with increased λ_{Edd} , as there may be other, more fundamental, drivers. To test for this, we performed a similar experiment as outlined at the end of Section 3.2.1, splitting the high- λ_{Edd} AGNs into bins of $L_{[\text{O III}]}$ and $L_{1.4\text{ GHz}}$ while controlling for λ_{Edd} . Unfortunately, there are too few AGNs in our highest λ_{Edd} bin (i.e. $\lambda_{\text{Edd}} > 0.3$) to perform a meaningful experiment (there are only six type 1 AGNs in our sample with $\lambda_{\text{Edd}} > 0.3$ and $L_{1.4\text{ GHz}} > 10^{23} \text{ W Hz}^{-1}$), so we resort to $\lambda_{\text{Edd}} > 0.1$.

⁴ There is a known correlation between the equivalent widths of the Fe II complex and λ_{Edd} , see Boroson & Green (1992) and Boroson (2002).

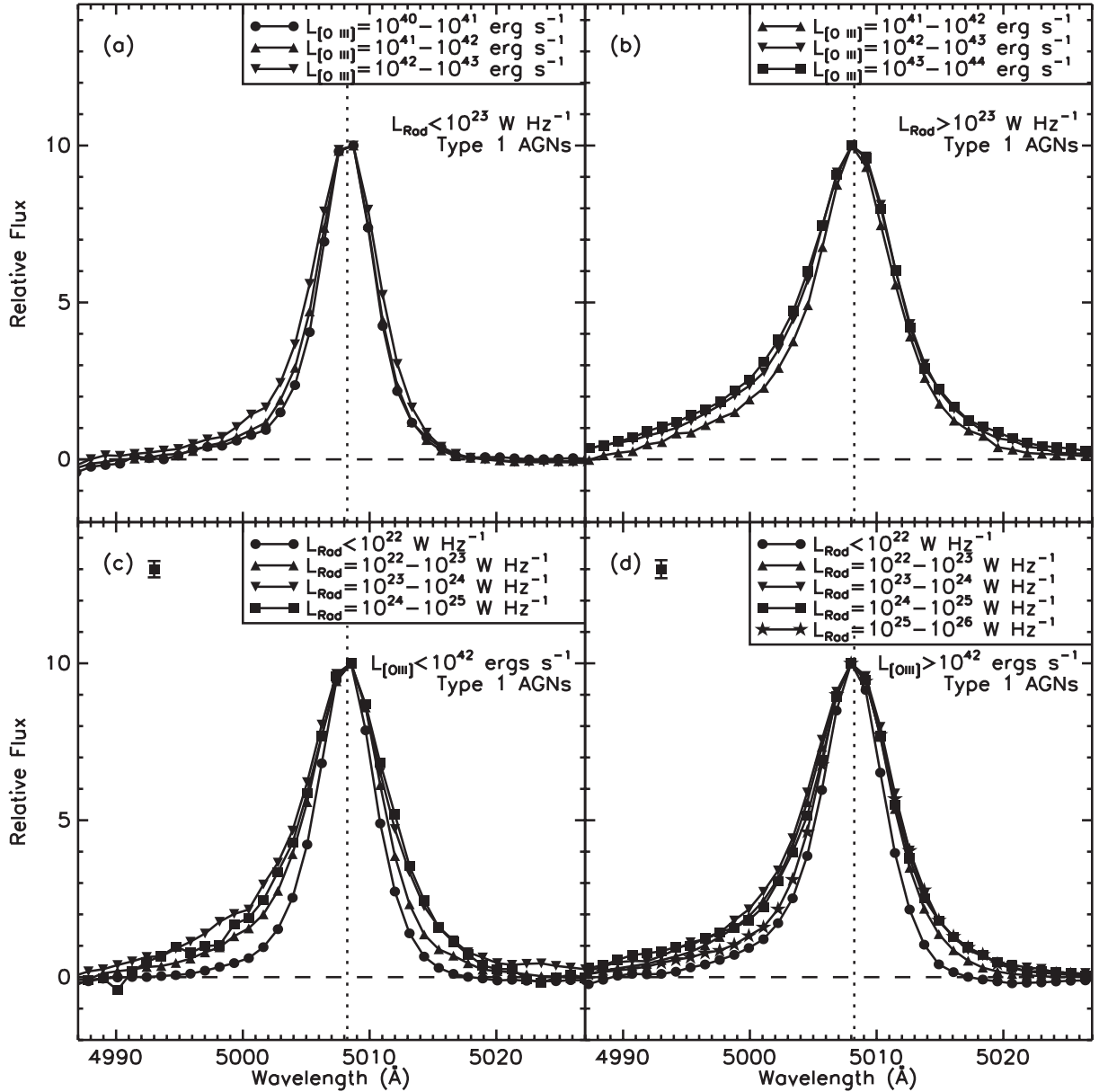


Figure 4. Average [O III] $\lambda 5007$ profiles of type 1 AGNs, accounting for the correlation between $L_{[\text{O III}]}$ and $L_{1.4 \text{ GHz}}$ in an attempt to isolate which has the greater effect on the line profiles. Panels (a) and (b) show the results of stacking as a function of $L_{[\text{O III}]}$, while keeping $L_{1.4 \text{ GHz}}$ roughly fixed (to $< 10^{23}$ and $10^{24} \text{ W Hz}^{-1}$, respectively). Alternatively, panels (c) and (d) show the results of stacking as a function of $L_{1.4 \text{ GHz}}$ keeping $L_{[\text{O III}]}$ roughly fixed (to $\sim 5 \times 10^{41}$ and $\sim 2 \times 10^{42} \text{ erg s}^{-1}$, respectively). The greatest change in the profiles of the [O III] $\lambda 5007$ line is seen when $L_{1.4 \text{ GHz}}$ is varied. As with Fig. 3 we show representative error bars when they are larger than the plotted points [see panels (c) and (d)].

The results of this experiment are shown in Fig. 5. As with the full type 1 AGN sample, we see a broadening of the [O III] $\lambda 5007$ line with $L_{[\text{O III}]}$ for $\lambda_{\text{Edd}} > 0.1$ AGNs, but note that these stacks have not been controlled for $L_{1.4 \text{ GHz}}$, so some of this broadening may be related to the correlation between $L_{[\text{O III}]}$ and $L_{1.4 \text{ GHz}}$. Indeed, we see a striking difference between the [O III] $\lambda 5007$ profiles of high- and low- $L_{1.4 \text{ GHz}}$ AGNs with high λ_{Edd} , suggesting that even in these high- λ_{Edd} AGNs, mechanical processes are playing an important role in the disturbing the [O III] $\lambda 5007$ emitting gas. However, we stress that this only applies to $\lambda_{\text{Edd}} > 0.1$ AGNs, as the small numbers of $\lambda_{\text{Edd}} > 0.3$ AGNs in our sample mean we cannot perform this experiment in the highest λ_{Edd} bin where we see the strongest blue wing.

3.2.3 Radio loudness and luminosity

In addition to radiative forces, it is also thought that radio jets (either compact or extended) may play a significant role in disturbing the interstellar medium around an AGN, potentially inducing feedback (e.g. Whittle 1992; Nelson & Whittle 1996; Tadhunter et al. 2001; Holt, Tadhunter & Morganti 2003, 2008). Indeed, Nesvadba et al. (2008) have suggested that the spatially resolved broadening of the [O III] $\lambda 5007$ lines in the spectra of high-redshift radio galaxies is the result of interactions between a radio jet and the NLR. If this is the case, then we may expect the profiles of the [O III] $\lambda 5007$ line to be related to the radio properties of the AGNs.

In the lower two panels of Fig. 3, we present the average [O III] $\lambda 5007$ profiles of the type 1 AGNs in our sample, stacked

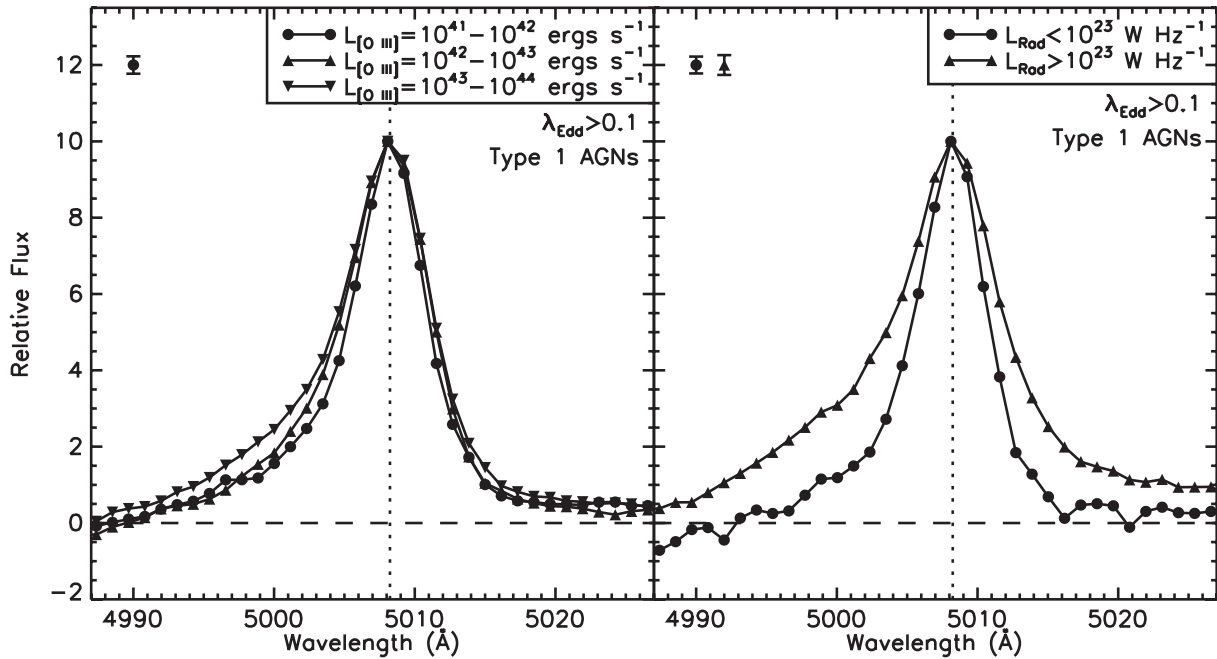


Figure 5. Average [O III] $\lambda 5007$ profiles of high-Eddington-ratio ($\lambda_{\text{Edd}} > 0.1$) type 1 AGNs, split as a function of [O III] $\lambda 5007$ luminosity (left) and radio luminosity (right). Similar to Fig. 4, we have stacked in different $L_{[\text{O III}]}$ and $L_{1.4\text{ GHz}}$ bins (see keys), matching λ_{Edd} in each bin to keep the average λ_{Edd} roughly the same between the two bins. As with Fig. 3 we show representative error bars when they are larger than the plotted points.

according to radio loudness (defined here as $R_{\text{Rad}} = F_{1.4\text{ GHz}}/F_B$, where $F_{1.4\text{ GHz}}$ and F_B are the flux densities measured in the 1.4 GHz band and the rest-frame optical B band, respectively) and radio luminosity (at 1.4 GHz; hereafter $L_{1.4\text{ GHz}}$).⁵ The average [O III] $\lambda 5007$ profiles show evidence of only a modest change across over three orders of magnitude in R_{Rad} (i.e. $R_{\text{Rad}} < 10$ to 10^3 – 10^4). As an aside, we find that the average [O III] $\lambda 5007$ lines of radio-detected (irrespective of loudness) AGNs have profiles similar to those AGNs with the highest $L_{[\text{O III}]}$ values (i.e. $L_{[\text{O III}]} > 10^{42}$ erg s^{−1}). However, this result is not surprising when we consider that the radio-detected AGNs in our sample typically have high [O III] $\lambda 5007$ luminosities. For example, 75 percent (i.e. 654/871) of radio-detected type 1 AGNs have $L_{[\text{O III}]} > 10^{42}$ erg s^{−1}.

We also investigated whether any trend exists between the average [O III] $\lambda 5007$ profile and radio luminosity (as opposed to radio loudness). From our spectral stacks we find that there is a non-monotonic change in the average [O III] $\lambda 5007$ profiles over the four orders of magnitude range in $L_{1.4\text{ GHz}}$ spanned by our sample; the $L_{1.4\text{ GHz}} = 10^{23}$ – 10^{24} and 10^{24} – 10^{25} W Hz^{−1} stacks display a marginally stronger blue wing compared to the $L_{1.4\text{ GHz}} = 10^{22}$ – 10^{23} and 10^{25} – 10^{26} W Hz^{−1} stacks.

As outlined in Section 3.2.1, it is important that we consider the influence that the correlation between $L_{[\text{O III}]}$ and $L_{1.4\text{ GHz}}$ may have on our results. For this, we employ a similar method as that used in Section 3.2.1. This time, however, we control for $L_{[\text{O III}]}$ while stacking as a function of $L_{1.4\text{ GHz}}$, ensuring that the median $L_{[\text{O III}]}$ of the stacked sources are consistent to within a factor of 3. The results of this experiment are shown in the lower two panels of Fig. 4. Here, we have separated the sample into high and low [O III] $\lambda 5007$ luminosity subsamples (i.e. $L_{[\text{O III}]} > 10^{42}$ and $< 10^{42}$ erg s^{−1}, respectively). In both subsamples, we see a clear change in the average [O III] $\lambda 5007$

line profiles as a function of $L_{1.4\text{ GHz}}$. We note again, however, that this increase is not monotonic. Instead, the [O III] $\lambda 5007$ profile broadens with increasing $L_{1.4\text{ GHz}}$ from $L_{1.4\text{ GHz}} < 10^{22}$ to 10^{23} – 10^{24} W Hz^{−1} ($L_{1.4\text{ GHz}} = 10^{23}$ – 10^{25} W Hz^{−1} in the case of $L_{[\text{O III}]} > 10^{42}$ erg s^{−1} AGNs), but then decreases in width as $L_{1.4\text{ GHz}}$ increases further (to $L_{1.4\text{ GHz}} = 10^{24}$ – 10^{25} and 10^{25} – 10^{26} W Hz^{−1} for the $L_{[\text{O III}]} < 10^{42}$ and $L_{[\text{O III}]} > 10^{42}$ erg s^{−1} subsamples, respectively).

3.2.4 The average [O III] $\lambda 5007$ profiles of NLS1s

It has previously been suggested that type 1 AGNs with narrow Balmer lines (i.e. < 4000 km s^{−1}) and, in particular, NLS1s show a tendency to have more prominent [O III] $\lambda 5007$ blue wings or blueshifts compared to BLS1s (e.g. Marziani et al. 2003; Komossa et al. 2008) – a feature previously attributed to the higher Eddington ratios of NLS1s. We can test for this using our sample of type 1 AGNs. In Fig. 6, we present the stacked [O III] $\lambda 5007$ profile of the NLS1s in our sample compared against that of BLS1s. Here, we have stacked the same number of randomly selected BLS1s as there are NLS1s in our sample (i.e. 1096). We find no significant difference between the average [O III] $\lambda 5007$ profiles of BLS1s and NLS1s in our sample. As a check, we also show in this plot the stacked H α profiles, confirming that our sample of NLS1s does, indeed, have significantly narrower permitted emission lines (i.e. broad-component FWHM_{H α} of 4460 and 1590 km s^{−1}; typical for these respective classes of object). Furthermore, the NLS1s in our sample have systematically higher Eddington ratios than their BLS1 counterparts, as highlighted in the inset plot showing the distribution of λ_{Edd} for the BLS1 and NLS1 samples. Finally, we note that the profile of the stacked [O III] $\lambda 5007$ is largely independent of our criteria for identifying NLS1s; there is no significant change in the [O III] $\lambda 5007$ profile when we change our NLS1 selection criteria to FWHM_{H α} < 1500 or < 2500 km s^{−1}; in other words the average [O III] $\lambda 5007$ profile is not dominated by NLS1 AGNs with

⁵ B -band fluxes were calculated by passing the rest-frame SDSS spectra through a synthetic Buser B -band response filter.

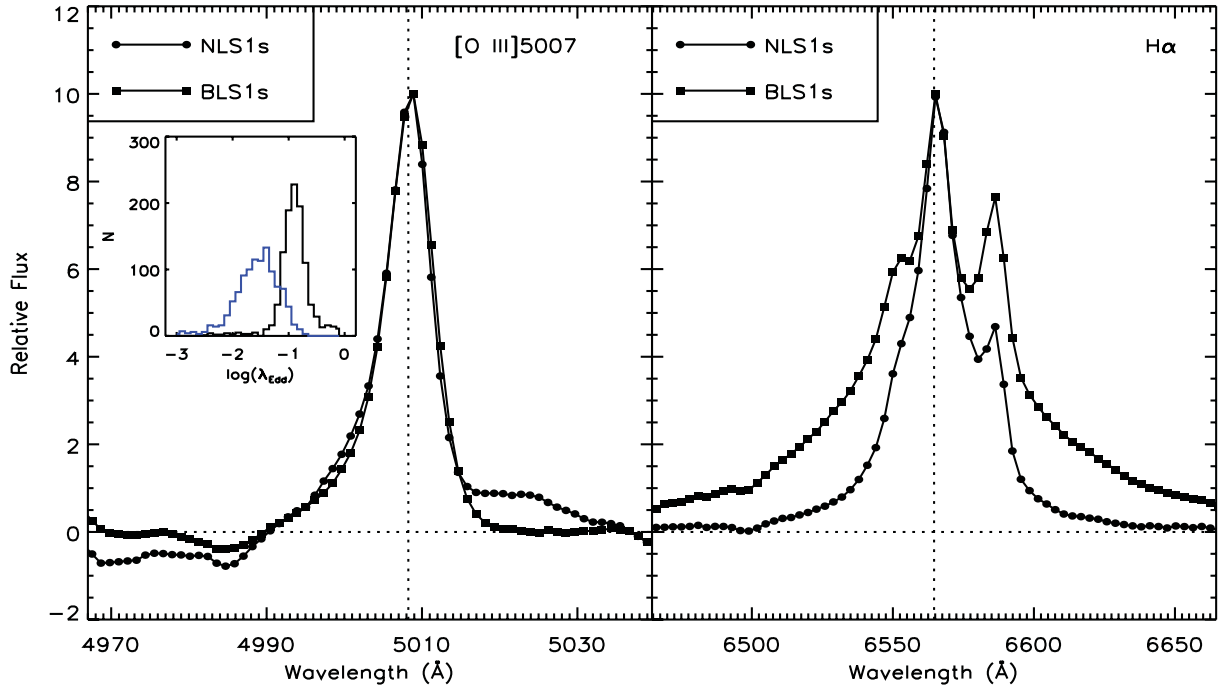


Figure 6. Average [O III] $\lambda 5007$ profile (left) and H α profile (right) of the BLS1 and NLS1 AGNs in our sample. Inset: the distribution of Eddington ratios for the NLS1s (black histogram) and the BLS1s (blue histogram) in our sample, indicating that the NLS1s have systematically higher Eddington ratios. We find no evidence to suggest that, on average, NLS1s have [O III] $\lambda 5007$ lines that are either broader or more blueshifted than their BLS1 counterparts.

$\text{FWHM}_{\text{H}\alpha}$ close to the (arbitrary) boundary between NLS1s and BLS1s.

3.3 Comparison of [O III] $\lambda 5007$ profiles of type 1 and type 2 AGNs

Up to this point, we have only considered the [O III] $\lambda 5007$ profiles of type 1 AGNs. The observed differences between type 1 and type 2 AGNs are now generally regarded as being the result of obscuration caused by gas and dust along our line of sight to their central regions (e.g. Antonucci 1993). It is therefore of interest to consider type 2 AGNs in order to gain insight into the role that AGN orientation and obscuration plays in the profiles of the [O III] $\lambda 5007$ emission lines.

In Fig. 7, we present the average [O III] $\lambda 5007$ profile derived from stacking all 13 713 type 2 AGNs in our sample. For comparison, we also include the average [O III] $\lambda 5007$ profile of the type 1 AGNs in our sample (presented previously in Fig. 2). Compared to the average [O III] $\lambda 5007$ profile of the type 1 AGNs, the type 2s display a less prominent blue wing (i.e. is more symmetrical). Since the [O III] $\lambda 5007$ line broadens with increasing $L_{[\text{O III}]}$ (but see Section 3.2.3), the narrower type 2 profile may in part be the result of the lower average $L_{[\text{O III}]}$ of the type 2 AGNs in our sample compared to type 1s (due to dilution from the strong continuum in the latter; median $L_{[\text{O III}]}$ = 6×10^{41} and 1.8×10^{42} erg s $^{-1}$, respectively). Having said that, as with the stacks of the type 1 AGNs, the [O III] $\lambda 5007$ profiles type 2 AGNs become increasingly broad with increasing $L_{[\text{O III}]}$, but remain more symmetric than the type 1 stacked profiles, as recently reported by Vaona et al. (2012) (see Fig. 8, left-hand panel). Similarly, we note that the [O III] $\lambda 5007$ profiles of the type 2 AGNs follow roughly the same trend with $L_{1.4\text{GHz}}$ as the type 1s (i.e. increasing in width to $L_{1.4\text{GHz}} = 10^{23}$ – 10^{24} W Hz $^{-1}$, then narrowing to higher $L_{1.4\text{GHz}}$) while, again, remaining more symmetrical

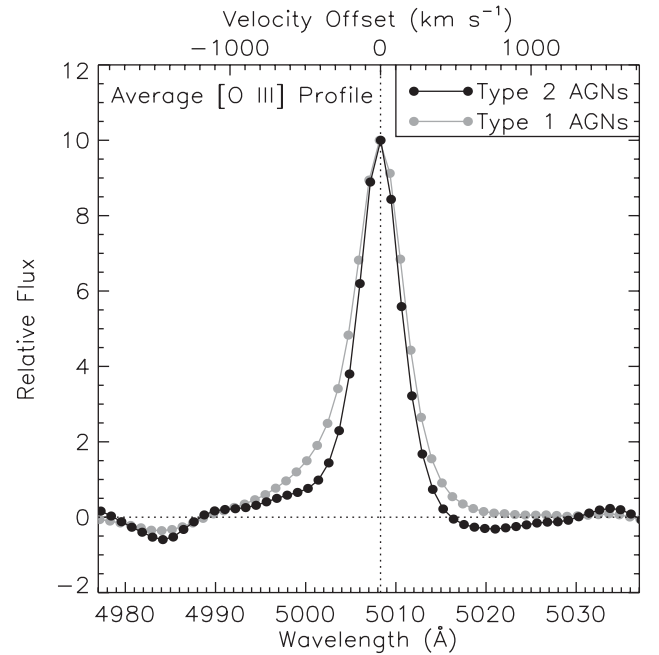


Figure 7. Average [O III] $\lambda 5007$ profile of the type 2 AGNs in our sample, derived from spectral stacking. This average profile shows less prominent blue wings compared to the average type 1 profile (shown in grey). The absorption on either side of the [O III] $\lambda 5007$ line is attributable to the stellar features in the host galaxy component which are stronger in type 2 AGNs due to the central engine continuum being obscured from view.

(see Fig. 8, right-hand panel). The more symmetrical [O III] $\lambda 5007$ profiles of type 2 AGNs are expected if the central engine is driving an [O III] $\lambda 5007$ emitting outflow along the axis perpendicular to the plane of the obscuring torus. In this model, orientation effects

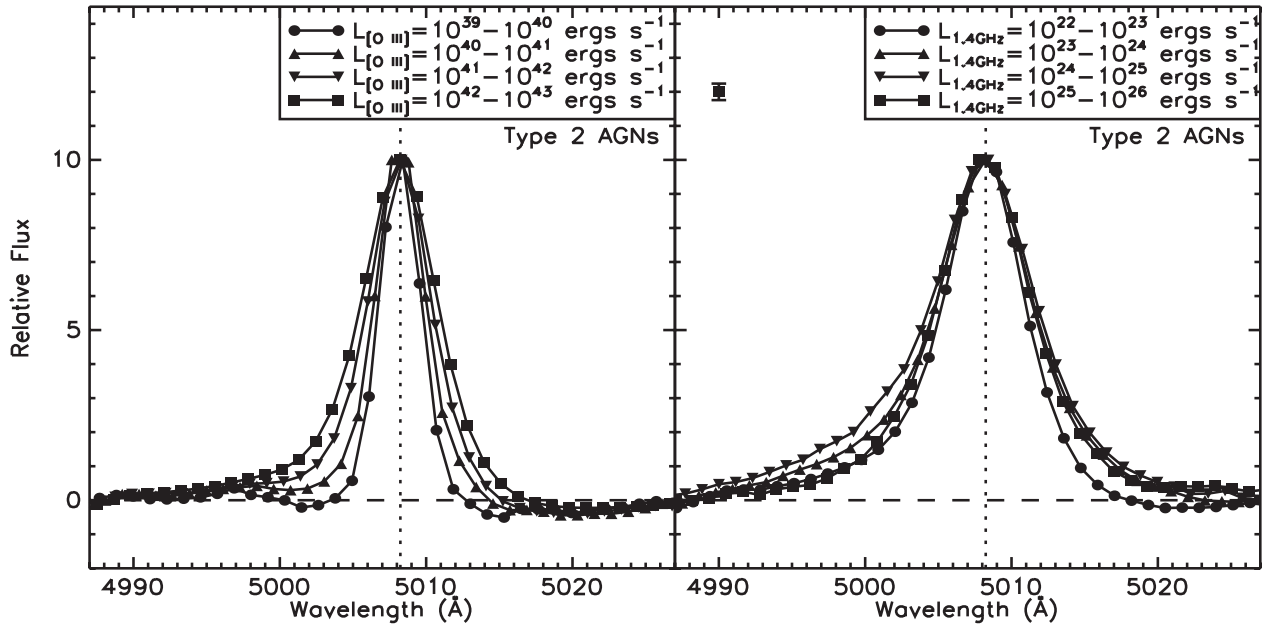


Figure 8. Average [O III] $\lambda 5007$ profiles of type 2 AGNs binned according to [O III] $\lambda 5007$ luminosity (left) and radio luminosity (right). As is the case for type 1 AGNs (see Fig. 2), we find that the average [O III] $\lambda 5007$ profile of type 2 AGNs increases in width with increasing [O III] $\lambda 5007$ luminosity. However, the type 2 profiles show much less prominent blueward asymmetries compared to the average [O III] $\lambda 5007$ profiles of type 1 AGNs. As with Fig. 3 we show representative error bars when they are larger than the plotted points.

mean that outflows from type 1 (i.e. unobscured) AGNs will appear more strongly blueshifted than those from type 2 (i.e. obscured) AGNs. This is consistent with Harrison et al. (2012), who reached the same conclusion using spatially resolved (i.e. integral field unit) spectroscopy.

4 RESULTS FROM INDIVIDUAL EMISSION-LINE FITS

We have shown that the average [O III] $\lambda 5007$ emission-line profile of optically selected type 1 AGNs displays a strong blue wing and that, once the correlation between $L_{[\text{O III}]}$ and $L_{1.4\text{GHz}}$ has been taken into account, the width of the average [O III] $\lambda 5007$ is most strongly related (though not in a monotonic sense) to the radio luminosity of the AGN. We see no evidence that the average profile of the [O III] $\lambda 5007$ line changes strongly as a function of radio loudness or Eddington ratio, and find that $L_{[\text{O III}]}$ (assumed to be a proxy for L_{AGN}) has a relatively minor impact on the average profile (compared to the radio luminosity). There is no difference in the average [O III] $\lambda 5007$ profiles of BLS1s and NLS1s, while type 2 AGNs have, on average, more symmetric [O III] $\lambda 5007$ emission lines compared to type 1s but their widths follow the same general trends.

In this section, we further explore the results derived from the spectral stacks by using the results from our fits to the [O III] $\lambda 5007$ emission line of the individual spectra in our AGN sample. In doing so, we will demonstrate that the vast majority of all AGNs have relatively narrow average [O III] $\lambda 5007$ profiles, while it is the AGNs with $10^{23} < L_{1.4\text{GHz}}/\text{WHz}^{-1} < 10^{25}$ that dominate the numbers with the broadest [O III] $\lambda 5007$ lines.

We use the results from our multicomponent fitting routine to quantify the proportions of optically selected AGNs with broadened [O III] $\lambda 5007$ lines. Our fitting routine fits up to two Gaussian components to the [O III] $\lambda 5007$ lines. However, rather than focusing on

the properties of single components, we calculate the flux-weighted average FWHM of the [O III] $\lambda 5007$ line:

$$\text{FWHM}_{\text{Avg}} = ((\text{FWHM}_A F_A)^2 + (\text{FWHM}_B F_B)^2)^{\frac{1}{2}}, \quad (2)$$

where F_A and F_B are the fractional fluxes contained within the two fitted components, A and B. By primarily focusing on average FWHMs, we avoid arbitrary definitions such as the threshold above which a broad component constitutes an important contribution to the overall flux of the emission line, or the point beyond which a component is considered ‘broad’. This characterization of the width of the [O III] $\lambda 5007$ line also ensures that all AGNs, whether their [O III] $\lambda 5007$ lines fitted either with one or two Gaussians, can be compared on an equal footing (i.e. including, for example, AGNs in which the [O III] $\lambda 5007$ line is broad, but satisfactorily fitted with a single Gaussian).

By measuring the [O III] $\lambda 5007$ profiles of individual AGNs we can quantify our sample in terms FWHM_{Avg} . In Fig. 9, we show the fractions of our sample with FWHM_{Avg} above a given value. It is clear that AGNs with relatively narrow [O III] $\lambda 5007$ lines dominate our sample, with the two-thirds of all AGNs having $\text{FWHM}_{\text{Avg}} < 400 \text{ km s}^{-1}$. The median FWHM_{Avg} of $L_{[\text{O III}]} > 10^{42} \text{ erg s}^{-1}$ AGNs is marginally higher than that of our whole AGN sample (~ 340 and $\sim 330 \text{ km s}^{-1}$), although this may in part be due to a broad component being easier to identify among the higher S/N spectra of these high- $L_{[\text{O III}]}$ AGNs. Approximately 17 per cent of all AGNs in our sample have $\text{FWHM}_{\text{Avg}} > 500 \text{ km s}^{-1}$, which is roughly the lower FWHM limit adopted by previous studies of AGN outflows when selecting targets for follow-up resolved (i.e. long-slit or integral field) spectroscopic studies of AGN outflows (see fig. 1 of Harrison et al. 2012). Also shown in Fig. 9 is the cumulative fraction for $L_{1.4\text{GHz}} > 10^{23} \text{ WHz}^{-1}$ AGNs, which indicates that the incidence of extremely broad [O III] $\lambda 5007$ lines (i.e. $\text{FWHM}_{\text{Avg}} > 1000 \text{ km s}^{-1}$) is approximately five times higher among these radio luminous AGNs than among AGNs in general (although the

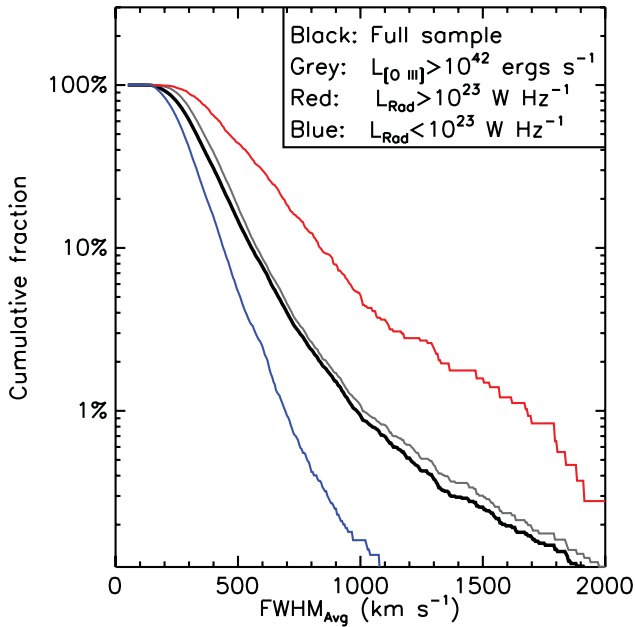


Figure 9. The fraction of AGNs in our samples with FWHM_{Avg} greater than a given value (shown on the abscissa). $[\text{O III}] \lambda 5007$ lines with $\text{FWHM}_{\text{Avg}} > 1000 \text{ km s}^{-1}$ are approximately five times more prevalent among AGNs with $L_{1.4 \text{ GHz}} > 10^{23} \text{ W Hz}^{-1}$ compared to the overall AGN population. We have included upper limits in the $L_{1.4 \text{ GHz}} < 10^{23} \text{ W Hz}^{-1}$ sample when they are consistent with this limit.

fractions are still small; e.g. ~ 5.5 per cent and ~ 1.1 , respectively, have $\text{FWHM}_{\text{Avg}} > 1000 \text{ km s}^{-1}$.

In Fig. 10 we plot the distribution of FWHM_{Avg} as a function of $L_{[\text{O III}]}$. In the leftmost panel, we plot all AGNs in our sample (including both type 1 and type 2 AGNs). As expected from the cumulative fractions (Fig. 9), AGNs with $\text{FWHM}_{\text{Avg}} \lesssim 500 \text{ km s}^{-1}$ dominate this plot at all $L_{[\text{O III}]}$ values. The upper envelope of this distribution increases with $L_{[\text{O III}]}$ up to $L_{[\text{O III}]} \sim 10^{42} \text{ erg s}^{-1}$, although we reiterate that this may partly be explained by the low S/N of low-luminosity AGNs' spectra making it difficult to detect a broad emission-line component. Another possibility highlighted by the results of our spectral stacks is that this increase is driven by the $L_{[\text{O III}]} - L_{1.4 \text{ GHz}}$ correlation coupled with an increase in FWHM_{Avg} with $L_{1.4 \text{ GHz}}$. To test for this, we have split the sample according to $L_{1.4 \text{ GHz}}$ in the other two panels of Fig. 10 (showing $< 10^{23}$ and $> 10^{23} \text{ W Hz}^{-1}$ in the middle and right-hand panels, respectively). We include AGNs with upper limits on $L_{1.4 \text{ GHz}}$ (provided they are $< 10^{23} \text{ W Hz}^{-1}$) in the middle panel, but do not include any upper limits in the right-hand panel. Compared to the whole sample (i.e. left-hand panel), there is a distinct lack of $L_{1.4 \text{ GHz}} < 10^{23} \text{ W Hz}^{-1}$ AGNs with very broad FWHM_{Avg} , and the rise in upper envelope with $L_{[\text{O III}]}$ is much less pronounced. This difference is highly unlikely to be due to the smaller numbers in the $L_{1.4 \text{ GHz}} < 10^{23} \text{ W Hz}^{-1}$ sample compared the whole sample, with a KS test indicating a $\ll 0.1$ per cent chance that the two samples are drawn at random from the same underlying population.

The right-hand panel of Fig. 10 shows the FWHM_{Avg} versus $L_{[\text{O III}]}$ distribution for $L_{1.4 \text{ GHz}} > 10^{23} \text{ W Hz}^{-1}$.⁶ Despite there being

⁶ We note that the numbers of AGNs in the middle and right-hand panels do not sum to the numbers in the left-hand panel as there are significant numbers of AGNs in our sample with $L_{1.4 \text{ GHz}}$ upper limits $> 10^{23} \text{ W Hz}^{-1}$ which could not be reliably included in either the middle or right-hand plots.

far fewer sources in this plot overall compared to the middle panel, over seven times more of them lie at extreme values of FWHM_{Avg} (i.e. $> 1000 \text{ km s}^{-1}$; 59 compared to 8) and the entire distribution is centred around a higher FWHM_{Avg} . We find that FWHM_{Avg} shows no clear dependence on $L_{[\text{O III}]}$ for these radio luminous AGNs.

In the left-hand panel of Fig. 11 we plot FWHM_{Avg} against $L_{1.4 \text{ GHz}}$ to further explore the connection between these two parameters. We have included upper limits on $L_{1.4 \text{ GHz}}$ which dominate the numbers at $L_{1.4 \text{ GHz}} < 10^{24} \text{ W Hz}^{-1}$. The most striking aspect of this plot is the peak in the FWHM_{Avg} distribution around $L_{1.4 \text{ GHz}} = 10^{23} - 10^{25} \text{ W Hz}^{-1}$, which are the $L_{1.4 \text{ GHz}}$ associated with the broadest of our stacked $[\text{O III}] \lambda 5007$ profiles. As well as being traced by the detected sources, this peak is also defined by the upper limits on the radio-undetected sources. Furthermore, a KS test indicates that this distribution remains statistically the same if we restrict the sample to $z < 0.123$, at which point the flux limit corresponds to a maximum $L_{1.4 \text{ GHz}}$ of $10^{23} \text{ W Hz}^{-1}$, indicating that the distribution is not produced by a selection effect caused by the redshifts of the sources. At first sight this distribution suggests that moderate-luminosity radio AGNs are most effective at producing broad $[\text{O III}] \lambda 5007$ emission lines. However, other factors must first be ruled out before we can arrive at this conclusion as it is possible that a combination of selection effects could produce this distribution.

A possible explanation for the shape of the distribution at $L_{1.4 \text{ GHz}} < 10^{23} \text{ W Hz}^{-1}$ is that the correlation between $L_{1.4 \text{ GHz}}$ and $L_{[\text{O III}]}$ would make the broad component in these less radio luminous AGNs more difficult to detect by our line fitting procedure due to the weakness of the $L_{[\text{O III}]}$ line. However, when we reproduce the FWHM_{Avg} versus $L_{1.4 \text{ GHz}}$ plot using AGNs with $L_{[\text{O III}]} > 10^{42} \text{ erg s}^{-1}$ to ensure that any broad component is detected (Fig. 10 shows that any such detection bias is negligible at these $[\text{O III}] \lambda 5007$ luminosities), the same distribution is produced. As such, we can rule out this detection bias as having a major influence on the form of this distribution.

The small numbers of AGNs in our sample with $L_{1.4 \text{ GHz}} > 10^{25} \text{ W Hz}^{-1}$ may be the reason for the apparent drop-off in peak FWHM_{Avg} at these high $L_{1.4 \text{ GHz}}$. However, a KS test reveals that this is unlikely to be the case, returning only an ~ 0.05 per cent probability that the FWHM_{Avg} of $L_{1.4 \text{ GHz}} = 10^{24} - 10^{25} \text{ W Hz}^{-1}$ and $10^{25} - 10^{26}$ AGNs are drawn at random from the same underlying distribution. This and the arguments laid out above lead us to conclude that the peak in the $\text{FWHM}_{\text{Avg}} - L_{1.4 \text{ GHz}}$ distribution around $L_{1.4 \text{ GHz}} = 10^{23} - 10^{25} \text{ W Hz}^{-1}$ is unlikely to be due to selection effects and thus gives a true impression of the relationship between the profile of the $[\text{O III}] \lambda 5007$ emission line and the radio properties of the AGN.

5 DISCUSSION

In the previous sections we have explored how $[\text{O III}] \lambda 5007$ emission-line profiles differ between AGNs of different L_{AGN} (from $L_{[\text{O III}]}$), $L_{1.4 \text{ GHz}}$, λ_{Edd} and R_{Rad} . Since emission-line profiles are governed by the kinematics of the emitting gas, our results allow us to assess how the movement of gas surrounding the AGNs is related to these four key observables. In this section, we place our results in the context of previous studies of the kinematics of the $[\text{O III}] \lambda 5007$ emitting gas and, in doing so, consider the implications of our results on our understanding of how AGN-driven outflows influence galaxy growth.

The results from both our spectral stacks and our individual $[\text{O III}] \lambda 5007$ line fits show that, of the four observables considered

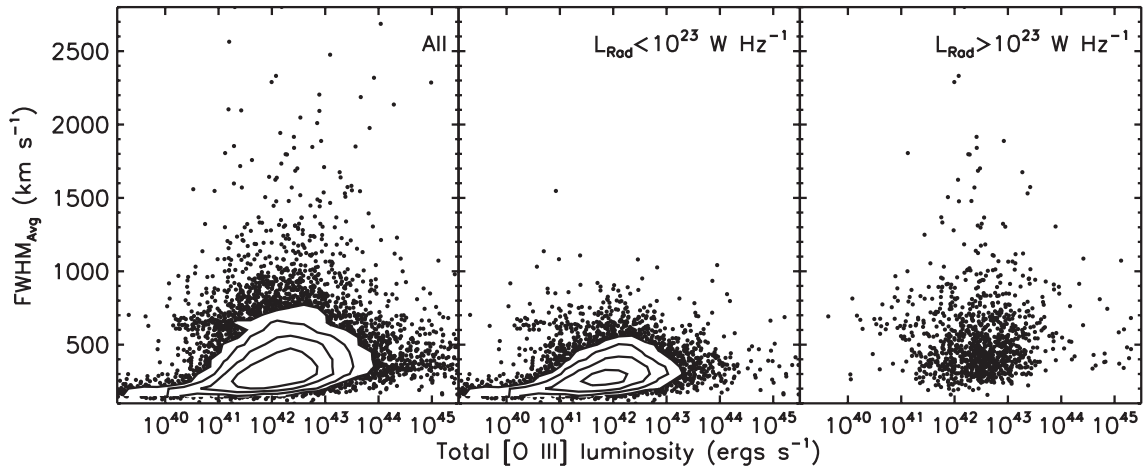


Figure 10. The distribution of FWHM_{Avg} (see equation 2) plotted as a function of $L_{[\text{O III}]}$ for all (left-hand panel), $L_{1.4\text{GHz}} < 10^{23} \text{ W Hz}^{-1}$ (middle panel) and $L_{1.4\text{GHz}} > 10^{23} \text{ W Hz}^{-1}$ (right-hand panel) AGNs. The upper envelope of this distribution peaks around $10^{42} \text{ erg s}^{-1}$. However, comparing the middle and right-hand panels reveals that the AGNs with the broadest tend to be the more radio luminous of our sample.

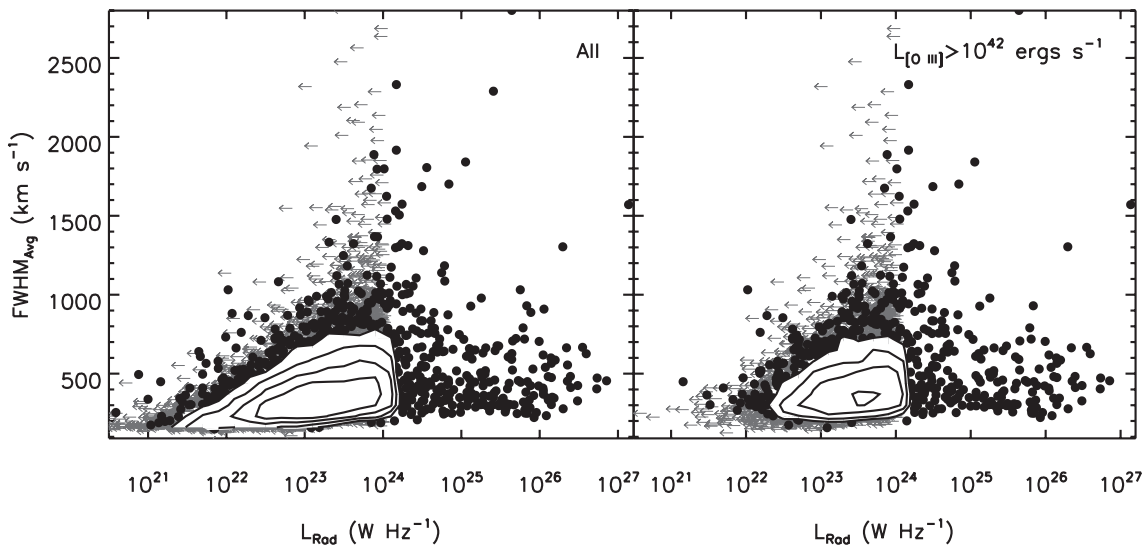


Figure 11. Distribution of FWHM_{Avg} plotted as a function of $L_{1.4\text{GHz}}$. The left-hand panel includes all of the AGNs in our sample, whereas the right-hand panel shows only those with $L_{[\text{O III}]} > 10^{42} \text{ erg s}^{-1}$. Both panels show a significant (i.e. 0.05 per cent chance of being produced by random) peak in the upper envelope of the distribution around $L_{1.4\text{GHz}} \sim 10^{24} \text{ W Hz}^{-1}$.

(i.e. L_{AGN} , $L_{1.4\text{GHz}}$, λ_{Edd} and R_{Rad}), $L_{1.4\text{GHz}}$ is the most important factor in dictating the profile of this emission line. Our results indicate that the width of the $[\text{O III}] \lambda 5007$ line peaks between $L_{1.4\text{GHz}} = 10^{23}$ and $\sim 10^{25} \text{ W Hz}^{-1}$ with both more and less radio powerful AGNs having, on average, narrower $[\text{O III}] \lambda 5007$ lines. Similar results were reported by Heckman et al. (1984) and Whittle (1992) for much smaller samples of AGNs. The size and relative completeness of our sample allow us to build on these previous studies, breaking the degeneracy between $L_{[\text{O III}]}$ and $L_{1.4\text{GHz}}$ to identify the underlying links, and placing AGNs with kinematically energetic NLRs in the context of the general population by quantifying the fraction with broad $[\text{O III}] \lambda 5007$ emission lines.

Spectral studies of small samples of AGNs displaying compact radio jets have reported broadened $[\text{O III}] \lambda 5007$ emission lines that are co-spatial with these jets (e.g. Tadhunter et al. 2003; Holt et al. 2006, 2008), suggesting that it is the jets' mechanical energy that is disturbing the $[\text{O III}] \lambda 5007$ emitting gas. Since we have no information regarding the spatial extent of the $[\text{O III}] \lambda 5007$ emitting

gas in our sample, we are unable to perform such a direct analysis here. Instead, we can exploit the spatial resolution of the FIRST radio survey to determine whether AGNs with broad $[\text{O III}] \lambda 5007$ have predominantly extended or compact radio morphologies. Taking NVSS-detected AGNs in our sample with $L_{1.4\text{GHz}} = 3 \times 10^{23} - 3 \times 10^{24} \text{ W Hz}^{-1}$ (to cover the peak of the FWHM_{Avg} distribution), we extract the angular extent of their radio major axis from the cross-matched FIRST catalogue, which has a higher spatial resolution at 1.4 GHz compared to NVSS. We find that all AGNs in this sample with $\text{FWHM}_{\text{Avg}} > 1500 \text{ km s}^{-1}$ and single FIRST matches have deconvolved extents $< 2 \text{ arcsec}$ (i.e. unresolved), and there is no evidence that more extended radio sources have broader $[\text{O III}] \lambda 5007$ lines. Furthermore, in the case of those with multiple FIRST matches, the vast majority of AGNs in this subsample (i.e. > 80 per cent) have at least one radio component closer than 1 arcsec to the galaxy nucleus, suggestive of a radio core. Finally, none of the AGNs in this radio-selected subsample have multiple NVSS matches, meaning that they are unlikely to have extended,

lobe-dominated radio emission without also having a compact core. While not conclusive, these various outcomes support the view that compact (i.e. \sim kpc scales or less) radio cores play a major, if not the dominant, role in strongly disturbing the [O III] λ 5007 emitting gas around optically selected AGNs. This may also explain why the [O III] λ 5007 width peaks at moderate $L_{1.4\text{GHz}}$, close to the division between Fanaroff–Riley types I and II, since the latter dissipate more of their energy at larger (i.e. \gg kpc) scales. However, we also point out that the peak of the FWHM_{Avg} distribution is close to the point at which the radio luminosity function becomes AGN, rather than star formation, dominated. It is therefore feasible that the radio output of some of the AGNs with the broadest [O III] λ 5007 lines is dominated by star formation.

One factor that we have not yet explored is the possibility that some of the AGNs in our sample may have boosted radio emission due to beaming, meaning that the intrinsic radio power may be considerably lower than what we infer here. However, while this may explain part of the decreased disturbance towards higher $L_{1.4\text{GHz}}$, it is unlikely that *all* (or even the majority) of the $L_{1.4\text{GHz}} \gtrsim 10^{25} \text{ W Hz}^{-1}$ AGNs in our sample are beamed (i.e. blazars), especially since emission-line selection would tend to bias *against* such AGNs as they tend to be continuum dominated (e.g. Morris et al. 1991; Stocke et al. 1991).

Our analyses show that a higher fraction of moderate-radio-luminosity (i.e. $L_{1.4\text{GHz}} = 10^{23} - 10^{25} \text{ W Hz}^{-1}$) AGNs display broad [O III] λ 5007 lines compared to either weaker or stronger radio AGNs. Furthermore, these fractions are only weakly dependent on L_{AGN} . These moderate- $L_{1.4\text{GHz}}$ AGNs represent roughly 3 per cent of optically selected AGNs at $z < 0.123$ (the redshift at which the NVSS survey is complete to $L_{1.4\text{GHz}} > 10^{23} \text{ W Hz}^{-1}$). As such, while they constitute a small fraction of optically selected AGNs overall, they are at least ~ 10 times more common than the more radio luminous AGNs that are typically the focus of detailed studies of AGN outflows (e.g. Holt et al. 2003, 2008; Tadhunter et al. 2003; Nesvadba et al. 2006, 2008; Cano-Díaz et al. 2012; see fig. 1 of Harrison et al. 2012 for a comparison). Those studies that have sampled the $L_{1.4\text{GHz}} \sim 10^{23} - 10^{25} \text{ W Hz}^{-1}$, $L_{[\text{O III}]} > 10^{42} \text{ erg s}^{-1}$ ranges have reported outflows extended over galaxy (i.e. \sim few kpc) scales, suggesting that they could be affecting their host galaxies (e.g. Greene et al. 2011; Harrison et al. 2012). A detailed comparison of the resolved radio components and the gas kinematics is required to determine whether (and, if so, how) the two are physically linked.

6 SUMMARY

We have used a large (i.e. 24 264) sample of optically selected AGNs from the SDSS data base to explore how the profiles of the forbidden [O III] λ 5007 emission line relate to other key AGN parameters (bolometric luminosity, Eddington ratio, radio loudness and radio luminosity). We use spectral stacking analyses to determine how the average [O III] λ 5007 profile changes as a function of these four parameters. We also explore the fractions of AGNs in each of these bins that have broad [O III] λ 5007 emission lines. Our main results can be summarized as follows.

(i) The average [O III] λ 5007 profile of type 1 AGNs displays a prominent blue wing that can be well described by a broad (i.e. $\text{FWHM} = 851 \text{ km s}^{-1}$) Gaussian component that is blueshifted by 148 km s^{-1} from a narrow (i.e. $\text{FWHM}_1 = 335 \text{ km s}^{-1}$) core. The flux contained within this broad component represents 45 per cent of the total average line flux (see Section 3.1).

(ii) When we separate the type 1 AGNs into discrete bins of $L_{[\text{O III}]}$ or Eddington ratio (λ_{Edd}), we find that the blue wings on the average [O III] λ 5007 profiles are increasingly prominent at higher values of $L_{[\text{O III}]}$ and in our highest λ_{Edd} bin (i.e. $\lambda_{\text{Edd}} > 0.3$; see Section 3.2.1 and Fig. 3). However, when we correct for the known correlation between $L_{[\text{O III}]}$ and $L_{1.4\text{GHz}}$, we find that $L_{1.4\text{GHz}}$ has the most profound effect on the [O III] λ 5007 profile, with $L_{1.4\text{GHz}} = 10^{23} - 10^{25} \text{ W Hz}^{-1}$ AGNs having the broadest profiles. This appears to be the case for high-Eddington-ratio AGNs (i.e. $\lambda_{\text{Edd}} > 0.1$), although we are not able to show this conclusively in our highest λ_{Edd} bin ($\lambda_{\text{Edd}} > 0.3$) due to the small number of such extreme AGNs even in our large sample.

(iii) There is no difference in the average [O III] λ 5007 profiles of BLS1 and NLS1 AGNs.

(iv) When the [O III] λ 5007 profiles of type 2 AGNs are stacked in terms of $L_{[\text{O III}]}$ their [O III] λ 5007 widths also increase with $L_{[\text{O III}]}$ but are more symmetric than those of type 1 AGNs. We interpret this as suggesting that the blue wings are the result of outflowing material directed roughly along the axis of the obscuring torus.

(v) Overall, roughly 25 per cent of all AGNs have average [O III] λ 5007 FWHM (i.e. $\text{FWHM}_{\text{Avg}} > 500 \text{ km s}^{-1}$), compared to ~ 50 per cent of AGNs with $L_{1.4\text{GHz}} > 10^{23} \text{ W Hz}^{-1}$. All of the AGNs in our sample with $\text{FWHM}_{\text{Avg}} \gtrsim 1200 \text{ km s}^{-1}$ have radio detections or upper limits consistent with $L_{1.4\text{GHz}} > 10^{23} \text{ W Hz}^{-1}$.

Acknowledging the limiting spatial resolution of the FIRST and NVSS surveys, our results are consistent with models in which compact radio cores play an important role in disturbing the diffuse gas around the AGN. Ascertaining whether the impact of these cores is felt on extended, galactic scales will require spatially resolved radio and spectroscopic observations.

ACKNOWLEDGEMENTS

JRM and DMA acknowledges The Leverhulme Trust. CMH acknowledges funding from STFC. This work has made use of data provided by the SDSS. Funding for the SDSS has been provided by the Alfred P. Sloan Foundation, the Participating Institutions, the National Science Foundation, the US Department of Energy, the National Aeronautics and Space Administration, the Japanese Monbukagakusho, the Max Planck Society and the Higher Education Funding Council for England. The SDSS website is <http://www.sdss.org/>.

REFERENCES

- Abazajian K. N. et al., 2009, *ApJS*, 182, 543
- Aird J. et al., 2010, *MNRAS*, 401, 2531
- Alexander D. M., Swinbank A. M., Smail I., McDermid R., Nesvadba N. P. H., 2010, *MNRAS*, 402, 2211
- Antonucci R., 1993, *ARA&A*, 31, 473
- Baldwin J. A., Phillips M. M., Terlevich R., 1981, *PASP*, 93, 5
- Bassani L., Dadina M., Maiolino R., Salvati M., Risaliti G., della Ceca R., Matt G., Zamorani G., 1999, *ApJS*, 121, 473
- Baum S. A., Heckman T., 1989, *ApJ*, 336, 702
- Best P. N., Kauffmann G., Heckman T. M., Brinchmann J., Charlot S., Ivezić Ž., White S. D. M., 2005, *MNRAS*, 362, 25
- Bian W., Gu Q., Zhao Y., Chao L., Cui Q., 2006, *MNRAS*, 372, 876
- Boroson T. A., 2002, *ApJ*, 565, 78
- Boroson T. A., Green R. F., 1992, *ApJS*, 80, 109
- Bower R. G., Benson A. J., Malbon R., Helly J. C., Frenk C. S., Baugh C. M., Cole S., Lacey C. G., 2006, *MNRAS*, 370, 645

Cano-Díaz M., Maiolino R., Marconi A., Netzer H., Shemmer O., Cresci G., 2012, *A&A*, 537, L8

Cardelli J. A., Clayton G. C., Mathis J. S., 1989, *ApJ*, 345, 245

Condon J. J., Cotton W. D., Greisen E. W., Yin Q. F., Perley R. A., Taylor G. B., Broderick J. J., 1998, *AJ*, 115, 1693

de Vries W. H., Hodge J. A., Becker R. H., White R. L., Helfand D. J., 2007, *AJ*, 134, 457

Di Matteo T., Springel V., Hernquist L., 2005, 433, 604

Feldman F. R., Weedman D. W., Balzano V. A., Ramsey L. W., 1982, *ApJ*, 256, 427

Goodrich R. W., 1989, *ApJ*, 342, 224

Greene J. E., Ho L. C., 2005a, *ApJ*, 627, 721

Greene J. E., Ho L. C., 2005b, *ApJ*, 630, 122

Greene J. E., Zakamska N. L., Ho L. C., Barth A. J., 2011, *ApJ*, 732, 9

Harrison C. M. et al., 2012, *MNRAS*, 426, 1073

Heckman T. M., Miley G. K., van Breugel W. J. M., Butcher H. R., 1981, *ApJ*, 247, 403

Heckman T. M., Miley G. K., Green R. F., 1984, *ApJ*, 281, 525

Heckman T. M., Ptak A., Hornschemeier A., Kauffmann G., 2005, *ApJ*, 634, 161

Ho L. C., Filippenko A. V., Sargent W. L. W., 1997, *ApJS*, 112, 315

Holt J., Tadhunter C. N., Morganti R., 2003, *MNRAS*, 342, 227

Holt J., Tadhunter C., Morganti R., Bellamy M., González Delgado R. M., Tzioumis A., Inskip K. J., 2006, *MNRAS*, 370, 1633

Holt J., Tadhunter C. N., Morganti R., 2008, *MNRAS*, 387, 639

Hopkins A. M., Beacom J. F., 2006, *ApJ*, 651, 142

Hopkins P. F., Hernquist L., Cox T. J., Di Matteo T., Robertson B., Springel V., 2006, *ApJS*, 163, 1

Husemann B., Wisotzki L., Sánchez S. F., Jahnke K., 2013, *A&A*, 549, A43

Ibar E., Ivison R. J., Best P. N., Coppin K., Pope A., Smail I., Dunlop J. S., 2010, *MNRAS*, 401, L53

Kauffmann G. et al., 2003, *MNRAS*, 346, 1055

Komossa S., Xu D., Zhou H., Storchi-Bergmann T., Binette L., 2008, *ApJ*, 680, 926

Maiolino R., Rieke G. H., 1995, *ApJ*, 454, 95

Marziani P., Zamanov R. K., Sulentic J. W., Calvani M., 2003, *MNRAS*, 345, 1133

Merloni A., Rudnick G., Di Matteo T., 2004, *MNRAS*, 354, L37

Morris S. L., Stocke J. T., Gioia I. M., Schild R. E., Wolter A., Maccacaro T., della Ceca R., 1991, *ApJ*, 380, 49

Nelson C. H., Whittle M., 1996, *ApJ*, 465, 96

Nesvadba N. P. H., Lehnert M. D., Eisenhauer F., Gilbert A., Tecza M., Abuter R., 2006, *ApJ*, 650, 693

Nesvadba N. P. H., Lehnert M. D., De Breuck C., Gilbert A. M., van Breugel W., 2008, *A&A*, 491, 407

Netzer H., Trakhtenbrot B., 2007, *ApJ*, 654, 754

Osterbrock D. E., 1981, *ApJ*, 249, 462

Pogge R. W., 1989, *ApJ*, 345, 730

Rawlings S., Saunders R., Eales S. A., Mackay C. D., 1989, *MNRAS*, 240, 701

Risaliti G., Maiolino R., Salvati M., 1999, *ApJ*, 522, 157

Rosario D. J., Shields G. A., Taylor G. B., Salvander S., Smith K. L., 2010, *ApJ*, 716, 131

Springel V., Di Matteo T., Hernquist L., 2005, *MNRAS*, 361, 776

Stocke J. T., Morris S. L., Gioia I. M., Maccacaro T., Schild R., Wolter A., Fleming T. A., Henry J. P., 1991, *ApJS*, 76, 813

Tadhunter C. N., Morganti R., Robinson A., Dickson R., Villar-Martin M., Fosbury R. A. E., 1998, *MNRAS*, 298, 1035

Tadhunter C., Wills K., Morganti R., Oosterloo T., Dickson R., 2001, *MNRAS*, 327, 227

Tadhunter C., Marconi A., Axon D., Wills K., Robinson T. G., Jackson N., 2003, *MNRAS*, 342, 861

Vaona L., Ciroi S., Di Mille F., Cracco V., La Mura G., Rafanelli P., 2012, *MNRAS*, 427, 1266

White R. L., Becker R. H., Helfand D. J., Gregg M. D., 1997, *ApJ*, 475, 479

Whittle M., 1985a, *MNRAS*, 213, 1

Whittle M., 1985b, *MNRAS*, 213, 33

Whittle M., 1992, *ApJ*, 387, 121

Wills K. A., Morganti R., Tadhunter C. N., Robinson T. G., Villar-Martin M., 2004, *MNRAS*, 347, 771

Wilson A. S., Willis A. G., 1980, *ApJ*, 240, 429

Wu Q., 2009, *MNRAS*, 398, 1905

Zhang K., Dong X.-B., Wang T.-G., Gaskell C. M., 2011, *ApJ*, 737, 71

Zirbel E. L., Baum S. A., 1995, *ApJ*, 448, 521

APPENDIX A: MULTICOMPONENT FITTING ROUTINE

The emission-line fitting procedure we have developed starts with a simple, single Gaussian fit to the [O III] $\lambda\lambda 4959, 5007$ emission lines and progresses by increasing the complexity of the fit until each line is fitted with multiple Gaussians where necessary. At each stage of the fitting procedure, any change in χ^2 is evaluated to establish whether the addition of any new Gaussian components has resulted in an improved fit (at a >99 per cent confidence level).

First, the procedure attempts to fit each of the [O III] $\lambda\lambda 4959, 5007$ emission lines simultaneously with single Gaussians. We require the FWHM and velocity offsets of these Gaussians to be equal throughout the fitting process and the normalization of the [O III] $\lambda 4959$ Gaussian fixed to 1/3 that of the [O III] $\lambda 5007$ Gaussian (i.e. $\text{FWHM}_{[\text{O III}]\lambda 4959} = \text{FWHM}_{[\text{O III}]\lambda 5007}$, $v_{[\text{O III}]\lambda 4959} = v_{[\text{O III}]\lambda 5007}$, $N_{[\text{O III}]\lambda 4959} = 1/3 \cdot N_{[\text{O III}]\lambda 5007}$). By fitting [O III] $\lambda 4959$ we minimize any influence both this and any neighbouring emission lines (e.g. the Fe II complexes) may have on the measurement of the [O III] $\lambda 5007$ profile. We note, however, that we do not use the results from fitting the [O III] $\lambda 4959$ in our analysis. The routine then attempts to fit each of the permitted H β and H α lines simultaneously with single Gaussians (referred to later as the ‘original’ H β and H α Gaussians), the velocity offsets and FWHM of which are, again, linked (i.e. $\text{FWHM}_{\text{H}\beta} = \text{FWHM}_{\text{H}\alpha}$, $v_{\text{H}\beta} = v_{\text{H}\alpha}$). Second Gaussians are then added to the fits of the [O III] $\lambda\lambda 4959, 5007$ lines in an attempt to model any complexities in the line profiles. The velocity, FWHM and normalization of this second set of [O III] $\lambda\lambda 4959, 5007$ Gaussians are linked in the same manner as the first set. Finally, the procedure attempts to fit the narrow components of the H β and H α lines and each of the [N II] $\lambda\lambda 6548, 6584$ lines with up to two further Gaussians, depending on whether the addition of the second [O III] $\lambda\lambda 4959, 5007$ Gaussians resulted in a significantly improved fit. Each of these additional Gaussians is forced to have the same velocity offsets and FWHM as their respective [O III] $\lambda\lambda 4959, 5007$ counterparts, but their relative normalizations are allowed to vary. We caution, however, that it has previously been reported that the line profiles of different forbidden species can differ (e.g. Komossa et al. 2008). By adopting the approach that the relative normalization of the two [O III] $\lambda 5007$ -derived narrow-line components can vary, we adopt a compromise between having some reasonable constraints on the fit to the permitted and [N II] $\lambda 6584$ lines (thus preventing these lines from broadening to accommodate the true broad permitted lines), while allowing the profile to vary somewhat to accommodate some of the differences between different species. The normalization of the [N II] $\lambda\lambda 6548$ line is fixed to 1/3 that of the [N II] $\lambda 6584$ line. In fitting the narrow components of the H β and H α lines with the modelled [O III] $\lambda\lambda 4959, 5007$ profile, the original H β and H α Gaussians are allowed to widen to fit any broad components of these permitted lines.

Since the goal of our fitting the emission-line profiles is to look for general trends within the large AGN population, we are not greatly concerned if a small number of ‘one off’ spectra are poorly fitted by

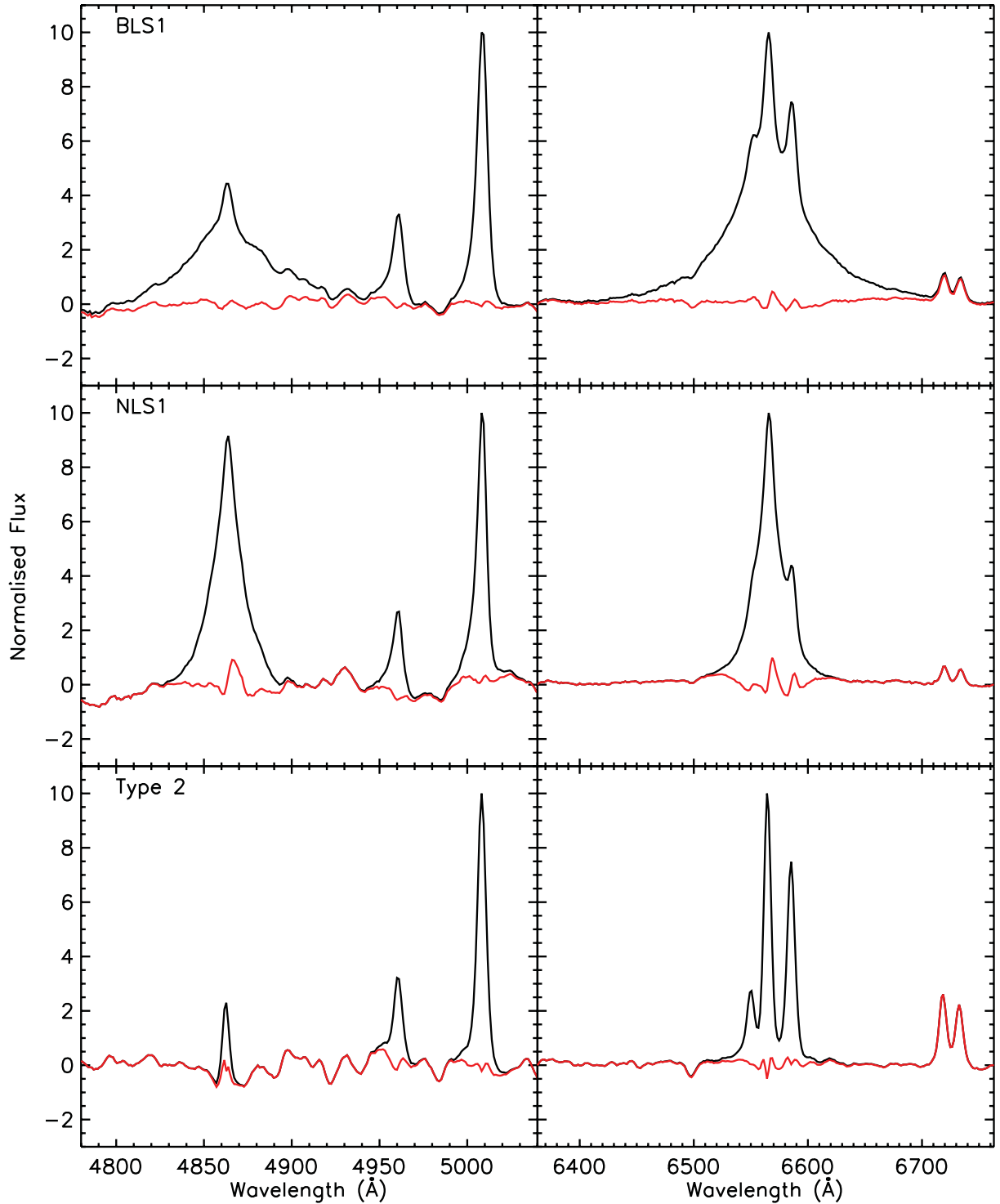


Figure A1. Stacked emission-line profiles (left: $H\beta$, $[O\text{ III}] \lambda 5007$; right: $H\alpha$) for 1000 BLS1s (top), NLS1s (middle) and type 2 (bottom) AGNs randomly selected from our full sample. The red lines show the results of stacking the spectra after subtracting the best-fitting line model [i.e. $\sum_i (F_i(\lambda) - F_i^{\text{model}}(\lambda))$].

We take the general lack of strong systematics in these average residual spectra as evidence that, over the sample, our line fitting routine is doing a reasonable job of modelling the profiles of the emission lines, particularly the broad wings of the $H\alpha$ and $H\beta$ lines and the overall $[O\text{ III}] \lambda 5007$ profile.

our routine, provided that it provides accurate fit parameters for the vast majority of sources in our sample. To demonstrate that this is the case, we plot the results of stacking randomly selected spectra after subtracting the best-fitting model (see the red line in Fig. A1).

We perform this for separate samples of BLS1s, NLS1s and type 2 AGNs, randomly selecting 1000 AGNs from each of these three samples. In general, we see only weak residuals around the fitted emission lines, especially the $[O\text{ III}] \lambda 5007$ lines (the bump around

the [O III] $\lambda 5007$ line in the NLS1 average spectrum is due to the Fe II complex which is stronger, in general, in this class of AGNs). There is evidence of a narrow residual in the H α and H β lines of the NLS1s (with a peak roughly 1/10th the maximum flux of these lines). However, since we only use the broad components of these lines to discriminate between NLS1s and BLS1s, which are

generally well fitted, this will not affect our main results. As such, we take these average residuals as evidence that, in general, our line fitting routine is providing an accurate and unbiased parametrization of the emission profiles of our sample spectra.

This paper has been typeset from a \TeX/L\AA\TeX file prepared by the author.